MULTICOMPONENT SEISMIC MONITORING OF THE EFFECTIVE STIMULATED VOLUME ASSOCIATED WITH HYDRAULIC FRACTURE STIMULATIONS IN A SHALE RESERVOIR, POUCE COUPE FIELD, ALBERTA, CANADA

by

Christopher Steinhoff

A thesis submitted to the Faculty and the Board of Trustees of the Colorado School of Mines in partial fulfillment of the requirements for the degree of Master of Science (Geophysics).

Golden, Colorado
Date ____________________

Signed: ____________________
Christopher Steinhoff

Signed: ____________________
Dr. Thomas L. Davis
Thesis Advisor

Golden, Colorado
Date ____________________

Signed: ____________________
Dr. Terence K. Young
Professor and Head
Department of Geophysics

ABSTRACT

The Reservoir Characterization Project in conjunction with Talisman Energy Inc., have been investigating a time-lapse data set acquired during hydraulic fracture stimulations of two horizontal wells in the Montney Shale at Pouce Coupe Field, Alberta, Canada. Multicomponent seismic surveys and microseismic data were acquired in December 2008 and integrated in this study with multiscale, multidisciplinary reservoir characterization techniques, including geomechanics and production data, to monitor changes within the reservoir associated with the hydraulic fracture stimulations.

The goal of this investigation was to study the feasibility of microseismic and time-lapse multicomponent seismic data for correlating hydraulic stimulation success to the enhanced permeability pathways created during the stimulation process. Three independently acquired microseismic monitoring surveys and the detected microseismic events were analyzed to infer the fracture length, height, azimuth, and asymmetry created by the hydraulic stimulation. Integrating the interpretation objectives with the multicomponent surface seismic processing sequence elevated the level of reservoir characterization that can be performed using the Pouce Coupe converted-wave seismic data. Shear-wave splitting as observed by the newly processed converted-wave data were sensitive to fracture induced anisotropy and therefore, provided a measurement of the dominant fracture orientation and fracture density difference within the Montney reservoir interval.

Before hydraulic stimulations, the natural fracture conditions resulted in a measured shear-wave splitting magnitude of 2-3%, with Baseline anomalies matching the independently interpreted minimal offset faults only visible on the converted-wave seismic data. Multistage hydraulic fracture stimulations increased the magnitude of shear-wave splitting up to 8%, well above the background noise level of 1%. The natural fractures and faults acted as conduits or barriers to the hydraulic stimulation energy causing a complicated stimulation response in the shear-wave splitting anomalies, due to the interaction between natural and hydraulic fractures. Characterizing the natural fractures and their failure tendencies can help drive the development of such a reservoir because fracture characteristics appeared to govern hydraulic stimulation success.

Conventional microseismic interpretation was deemed an unsatisfactory monitoring method of hydraulic fracture stimulations due to the limitation of only detecting the shear-failure events, representing a small amount of the total energy released during fracturing. The affected reservoir monitored by microseismic was concluded to not be characteristic of the volume contributing to production; therefore, the opening and propping of natural fractures were interpreted using shear-wave splitting monitoring and gave rise to a better representation of the effective stimulated volume. Finally, correlation of the overall shear-wave splitting anomalies to the stage-by-stage spinner production data concludes that shear-wave splitting monitoring better distinguishes the effective stimulated volume contributing to production.

TABLE OF CONTENTS

LIST OF FIGURES

LIST OF TABLES

ACKNOWLEDGEMENTS

I would like to first thank my advisor, Dr. Tom Davis for all his support on and off the ice, the Canadian connection and most importantly the friendship. Also, I would like to express my gratitude to the rest of my committee: Dr. Ilya Tsvankin for passing on his knowledge and appreciation of seismic anisotropy, and Eric Anderson and David D'Amico for their help and frankly I wouldn't be here without you.

My ever so grateful thanks are also extended to Heather Davey, you were the best partner, your brilliance is unrivalled and Geomechanics is now somewhat comprehensible. Furthermore, I thank Heather for pushing me as a colleague and most importantly as a friend.

The past year and a half of building this thesis was too enjoyable for words; the experiences were some of the best yet, and for this I owe too many thanks. Thank you Talisman Energy Inc. for the use of this incredible data set, Sensor Geophysical for all the processing efforts, particularly Jeff Grossman for dealing with the constant flood of emails. Also, Hampson-Russell for the software, and all the others who selflessly donated their time and resources, making this thesis what it is.

I would also like to thank the CSM Department of Geophysics for providing me with a "room" to "live" in, enlightening classes and so much more. Further thanking my CSM friends, fellow RCP'ers, and other Americans (primarily Ron Harris) because of you I am staying in the United States.

To all my friends back home in Canada, especially Darcy, Jordan, Kodie and Pamela, you are an extension of my family and I am so thankful for you all. I also owe a ton of recognition to the past Canadian RCP students and great friends of mine: Jared Atkinson and Kurt Wikel, thank you.

Most importantly, I must thank my family for their constant support, because of you two, Brandyn and Guy, I am who I am today. I love you both.

CHAPTER 1
INTRODUCTION

This thesis was part of an integrated study by the Reservoir Characterization Project that explores different scales of investigation to characterize the Montney Shale reservoir, Pouce Coupe Field, Alberta, Canada (Figure 1.1). Borehole scale geomechanics, engineering data (microseismic and reservoir tests) and production data were jointly analyzed with a time-lapse multicomponent seismic survey to determine the properties governing the effectiveness of hydraulic fracturing of the reservoir (Figure 1.2).

At the borehole scale, Davey (2012) conducted a geomechanical study to derive rock properties, natural fracture characteristics, the stress profile and the principal stresses, and the pressure conditions. Incorporating stress, the defined mechanical stratigraphy and Rock Quality Index (RQI), a geomechanical model was generated to determine how stress deforms and fractures rock. Natural fractures were characterized for orientations and dips, and used in a Mohr-Coulomb failure analysis to determine how the hydraulic stimulations would affect the reservoir. These hypotheses are crucial in interpreting the expected behavior in microseismic and time-lapse multicomponent monitoring.

In this thesis, seismic data were used at the field scale to characterize the geologic structure (thickness variations, faulting, etc.). Shear-wave splitting was used to determine the orientation and magnitude of in-situ natural fracturing and variations in the principal stresses over the field area. Monitoring the hydraulic stimulation with microseismic, time-lapse seismic and reservoir tests provides insight into how the heterogeneities within the reservoir control hydraulic energy dissipation.

1.1 Geology

The focus in this investigation is the Triassic Montney Shale reservoir, Canada (Figure 1.3). The Montney deposition extends over approximately 40,000 km^2 (13,000 km^2 of

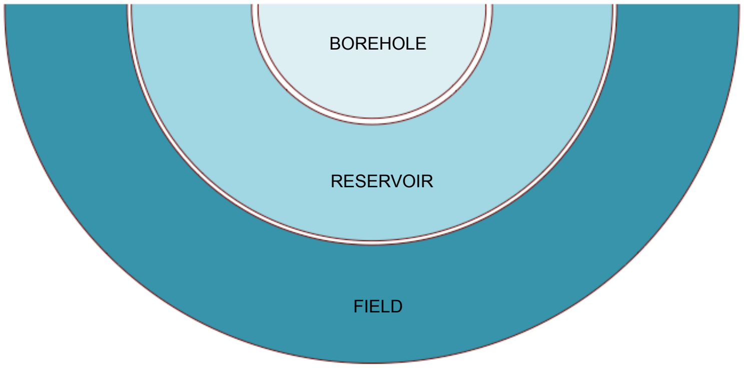

Figure 1.1: Reservoir characterization workflow - scales of characterization.

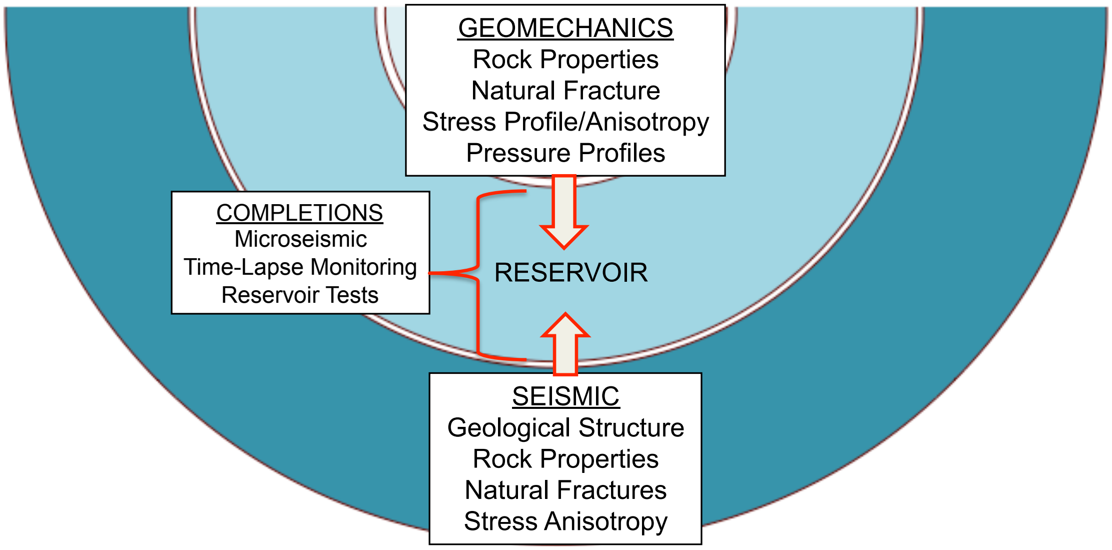

Figure 1.2: Geomechanics, seismic and stimulation monitoring for complete shale reservoir characterization. Showing the generalized scope of the Montney integrated study.

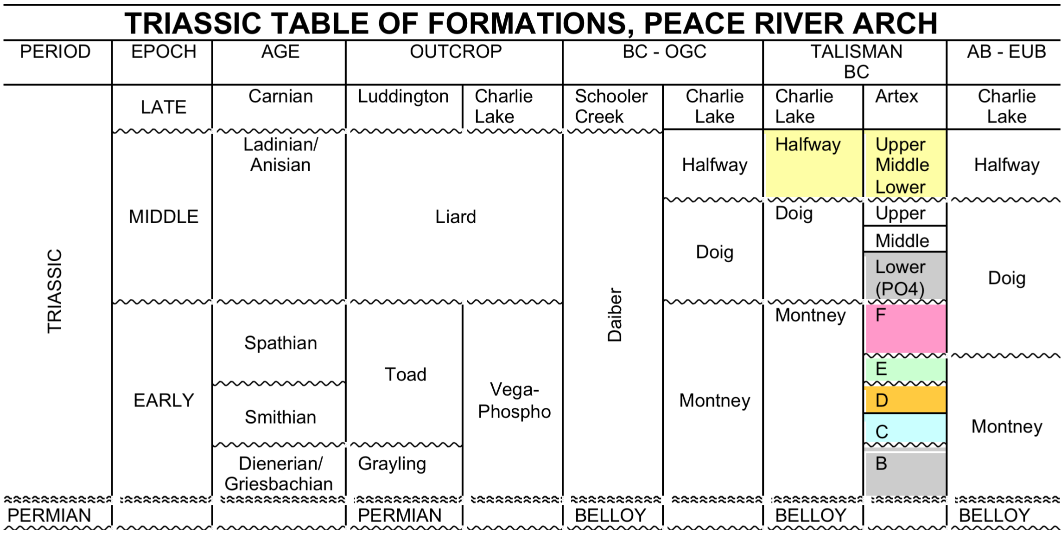

Figure 1.3: Triassic Montney Formation in the Peace River Arch region. Pouce Coupe Field is on the border of British Columbia (BC) and Alberta and is represented by the colored formations in the Talisman BC chart section (courtesy of Talisman Energy).

current focus) of the western margin of the Western Canadian Sedimentary Basin. The study area is Pouce Coupe Field, located on the British Columbia-Alberta border, in the Peace River area (Davies et al., 1997). Within the Peace River area the Montney Formation is generally classified as an organic-rich argillaceous siltstone and sandstone package, with fine-grained, pseudo-turbidites proximal to the shoreface deposition (Davey, 2012).

The Montney Formation unconformably overlies the Permian Belloy and it is overlain by the Middle Triassic Doig phosphate (Davies et al., 1997). Deposition of the Montney was controlled by the accommodation space of the western deepening embayment and the various grabens or paleostructures creating residual highs and lows on the Paleozoic surface (Davies et al., 1997). Fault reactivation and subsidence throughout the deposition of the Triassic strata continued to play a role in creation of the Montney reservoir. Maximum thickness of the Montney is approximately 350 meters with production depths ranging between 1700 and 2000 meters near Pouce Coupe Field.

The Pouce Coupe Field Montney has characteristic shale reservoir properties: a low matrix permeability of 0.01-0.02 mD and porosity 6-10% (Table 1.1). Permeability and porosity

Table 1.1: Montney reservoir properties compared to other North American shales. Pouce Coupe Field is located in the Montney Core area (information from Talisman Energy Inc.).

Parameters	Montney	Montney Core	Marcellus	Utica	Muskwa	Barnett
Permeability (nD)	130	20,000	250	160	230	300
Gas filled porosity (%)	2-5	7-9	1.6-7	2.5	1.6-7	3-5.5
Quartz and calcite (%)	50	60	17-36	20-55	12-69	13-50
Clays (%)	15	15	32	15	15	22
TOC (%)	1-5	0-1.5	1-12	0.2-2.2	1-10	3-8
Young's Modulus (GPa)	35-55	40-60	20-30	35-50	28-52	10-38

are comparatively lower due to the lack of pseudo-turbidites and the more distal deposition resulting in more shaley facies. The overall Montney package has characteristics similar to other shale reservoirs in North America, but with relatively higher values of porosity and permeability. The tight nature of the Montney reservoir requires enhanced permeability pathways of natural and induced fractures for economic production.

The Peace River deposition of the Montney, is further described in detail by Davies et al. (1997), Davey (2012), and Atkinson (2010).

1.1.1 Reservoir Units

The Montney package is subdivided from base into units A, B, C, D, E and F (Figure 1.4). The Lower Montney is comprised of units A, B and C, and is unconformably overlain by the Upper Montney. The Upper Montney contains the remaining units D, E and F. The upper units are typically separated from the lower units by a significant flooding surface.

Early field development was focused on the Upper Montney but with further developments in horizontal drilling technology expanded the producing intervals to both the C and D units; though the entire interval is commonly gas charged. Generally, Unit C contains reservoir-quality upward-coarsening shoreface and coarse siltstone facies. Unit D is represented by multicyclic, coarsening-upward siltstones and very fine sandstones with hummocky cross-stratification and local developments of thin dolomitized coquina facies (Davies et al., 1997).

The Lower Montney facies are depositionally controlled by the structural lows and highs

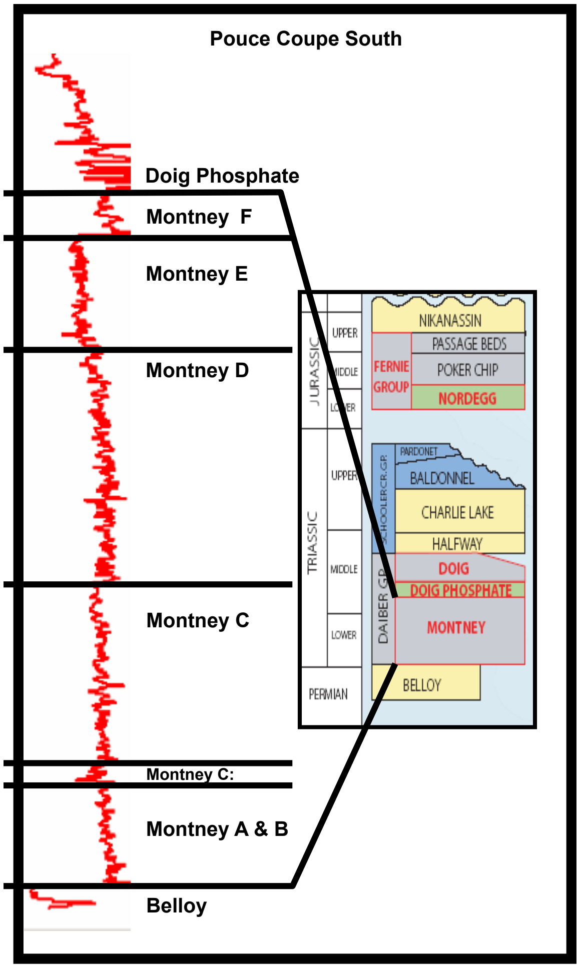

Figure 1.4: Type log of the Triassic Montney of the southern Pouce Coupe Field. The Montney package is subdivided from base into units A, B, C, D, E and F, and it overlain by the Doig Phosphate and unconformably underlain by the Permian Belloy. Red curve is the gamma ray.

of the Paleozoic surface and reach a maximum thickness of roughly 160 meters in the Pouce Coupe Field (Davies et al., 1997). The Upper Montney exhibits little structural influence on deposition and a maximum thickness of 230 meters (Davies et al., 1997).

Complete description of the sequence stratigraphy framework and interpretation can be seen in the work of Davey (2012).

1.1.2 Regional Tectonics

Both syn- and post-depositional faulting controlled the structure of the Montney. Graben complexes formed during the Triassic deposition were caused by the re-activation of NW-SE trending extensional basement faults, creating localized accommodation space variations. The Laramide orogeny represented a change in the stress regime from extensional to compressional and caused slip along many of the deeper basement faults (Figure 1.5). The tectonic history of this region has caused localized stress re-orientations, as seen near the maximum horizontal stress direction in the location of Pouce Coupe Field (Figure 1.6).

The present day regional stress regime of the Montney Shale reservoir is compressional with the regional maximum horizontal stress direction approximately N40^0E due to the Laramide orogeny (Late Cretaceous-Paleogene) forming the Canadian Rocky Mountains (Figure 1.6). The compressional stress regime is more completely described as strike-slip, characterized by the overburden stress (S_V) being the medial stress and the two horizontal stresses (S_H) representing the maximum and minimum stress magnitudes ($S_{Hmax}>S_V>S_{hmin}$). Variations in the differential horizontal stress ratio (S_{Hmax}/S_{hmin}) are significant and can greatly influence the reservoir geomechanical properties (Davey, 2012).

1.2 Field Development Background

The Montney Shale resource has been estimated to have a technically proven recoverable resource of 175 TcF, or 350 BcF per section. The reservoir has been exploited since 1993 with vertical wells and since 2005 with horizontal well technology. There are now upwards of 2,000 wells with 1,500 being horizontal. Still, with this amount of data and no company is above the challenges of developing such a reservoir, which is concluded by less then 60% of the wells are still producing (BMO, 2011).

The cumulative production from the Montney is estimated to be 2 TcF and 80% of the production coming from over 400 horizontal wells at a average rate of 1.6 Bcf/d in 2011. At this time there were six companies each with over 100 drilled horizontal wells. The Albertan

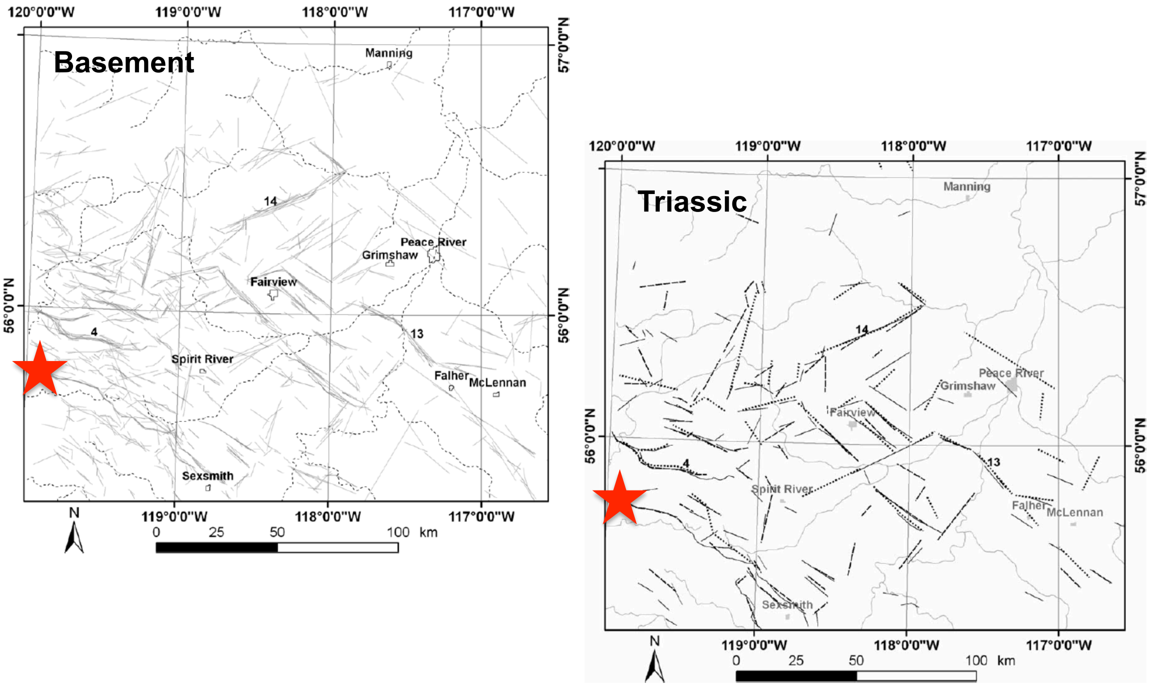

Figure 1.5: Basement and Triassic fault mapping in the Peace River Arch using refined well trend surface analysis (Mei, 2009). Major basement faults trend into the Triassic period. Pouce Coupe Field is shown by the red star.

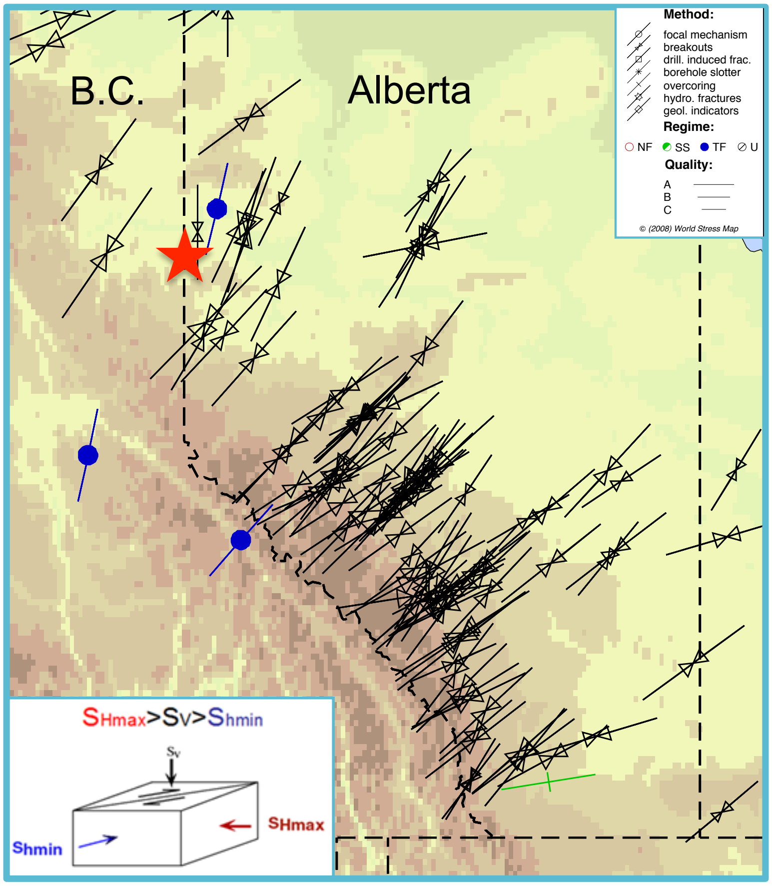

Figure 1.6: British Columbia-Alberta wellbore breakout deduced maximum horizontal stress orientations. The stress regime is generally characterized as strike-slip. Pouce Coupe Field is shown by the red star.

field development laws allow for horizontal wells to be drilled at a density of 12 wells per section, meaning the development of the Montney could reach upwards of 6,000 horizontal wells to tap the complete potential of the shale reservoir.

Two horizontal wells were drilled within the Pouce Coupe 4D-3C survey area targeting the Lower Montney unit C (102/02-07-078-10W6/00 referred to as the 2-07 well) and the lower Upper Montney unit D (102/07-07-078-10W6/00 referred to as the 7-07 well).

1.3 Hydraulic Stimulations

To enhance the economics and efficiency of gas production from shale reservoirs they must be completed using hydraulic stimulations or hydraulic fracturing. This process requires high pressure pumping of fluids into the reservoir interval to induce fractures and effectively connect permeability pathways to the wellbore. The permeability pathways must then be kept open using “proppant” typically comprised of sand.

Within the 3D seismic study area, the first horizontal well (2-07) was drilled and completed targeting the Montney C unit. Hydraulic stimulation was done individually on five 200 m-spaced perforation (stage) locations using an openhole packer system. The second horizontal well (7-07 well) targeted the Montney D unit and was stimulated with identical parameters as the first well (2-07 well), except at a constant interval spacing of 250 m (Table 1.2). “Clear Frac” fluids were used to induced hydraulic fractures and effectively transport proppant into the natural and induced void spaces. Each well was allowed to flow back after the hydraulic stimulation for long enough to retrieve the treatment balls at surface, and then shut-in to maintain pressure.

Since the stimulation practices were normalized it results in a meaningful comparison between the stage-by-stage stimulation success. Also, the differences can be attributed to variations in reservoir properties, including rock quality, presence of natural fractures and proximity to faults, and stress properties.

Table 1.2: Pouce Coupe Field horizontal well hydraulic stimulation parameters.

Date (m/d/y)	Well	Fluid Type	# of Stages/ Amt of Proppant	Proppant Size	H_2O Load (m^3)	Closure Pressure (MPa)
12-12-08	2-07	Clear Frac	5/100T	20/40	1328	30
12-17-08	7-07	Clear Frac	5/100T	20/40	1330	28

1.4 Thesis Data

In the Pouce Coupe Field Talisman Energy Inc. collected a wealth of data in December 2008. The complete set of data was acquired to test the feasibility of characterizing and monitoring hydraulic stimulations and production from a shale reservoir. The data consist of three time-lapse, multicomponent surveys, three independently acquired microseismic monitors, reservoir tests including production data and well log data to characterize and monitor changes within the Montney Shale reservoir.

In this section each of the data sets will be briefly introduced and main conclusions or limitations addressed.

1.4.1 Time-lapse, Multicomponent Seismic Data

Three time-lapse (4D), multicomponent (3C) surface seismic surveys were acquired by Talisman Energy Inc. at the Pouce Coupe Field, Alberta, Canada, in December 2008 (Figure 1.7). The seismic acquisition was designed to accurately characterize and monitor the Montney Shale reservoir using both compressional and converted-waves (P- and PS-waves, respectively).

The seismic data were recorded by CGGVeritas with Megabin geometry covering a typical patch of about 5 km^2 (1600 m by 3000 m). To achieve optimum acquisition repeatability the survey grid consists of 144 permanently buried 3C receivers (3.5 m depth) and 1241 cased shot holes (5.5 m depth). Acquisition configuration is represented in Figure 1.8 and the layout parameters in Table 1.3. Permanently installing the receivers and casing the dynamite shot holes with PVC guaranteed acquisition repeatability and confidence in detecting subtle

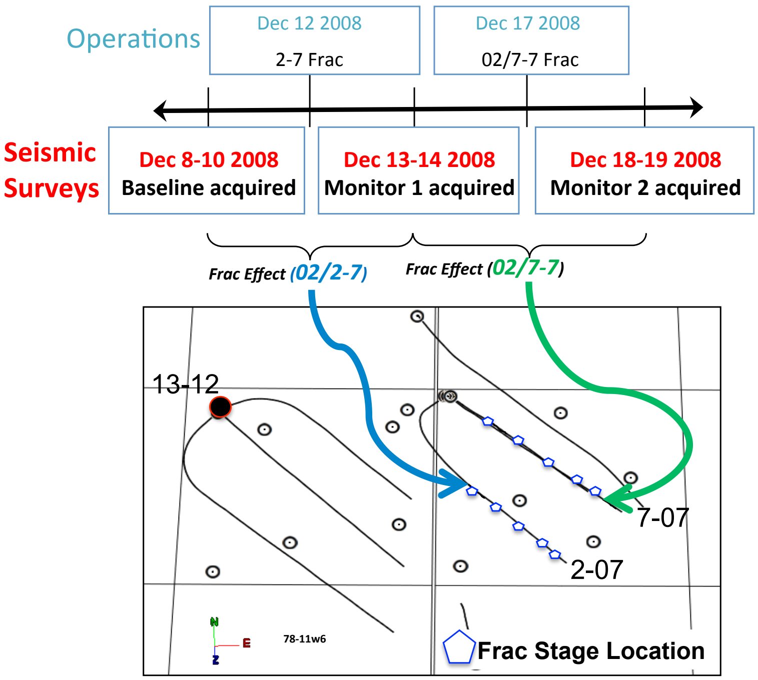

Figure 1.7: Pouce Coupe time-lapse, multicomponent surface seismic and field operations timeline. Two horizontal wells hydraulically stimulated (2-07 well and 7-07 well) and the location of the vertical shear sonic log (13-12 well). Modified from Atkinson (2010).

changes within the reservoir interval. The field layout resulted in 41 inlines and 101 crosslines. From the acquisition geometry the resulting bin size was 100 m by 100 m, but deemed unsatisfactory for our interpretation goals of determine the effective stimulation volume (expected to extend 250 m laterally) and the natural bin size was interpolated down to a 50 m by 50 m bin. The receivers recorded for 6 seconds at a sampling rate of 2 ms. Table 1.3 summarizes the survey acquisitions parameters.

The Baseline survey was acquired between December 8-10, 2008 to characterize the in-situ reservoir conditions before hydraulically fracturing the two horizontal wells. Two subsequent monitor surveys were acquired about 24 hours after the hydraulic stimulations operations took place and then shut in to retain pressure. The acquisition of the Monitor 1 and Monitor 2 took place between December 13-14 and 18-19, respectively, to investigate any time-lapse effects occurring due to the hydraulic fracture treatments of horizontal wells 2-07 and 7-07 (Figure 1.7).

Table 1.3: Pouce Coupe time-lapse, multicomponent seismic acquisition parameters.

Seismic Acquisition Parameters	
Recorded By	CGGVeritas
Survey Geometry	Megabin
Source Line Spacing	100 m
Receiver Line Spacing	200 m
Typical Patch	9 lines x 31 stations 1600m x 3000m
Charge Size (Dynamite)	Baseline: 0.5 Kg Monitor 1: 0.2 Kg Monitor 2: 0.2 Kg
Geophones	144 OYO Geospace 3C Nails
Sample Interval	2 ms

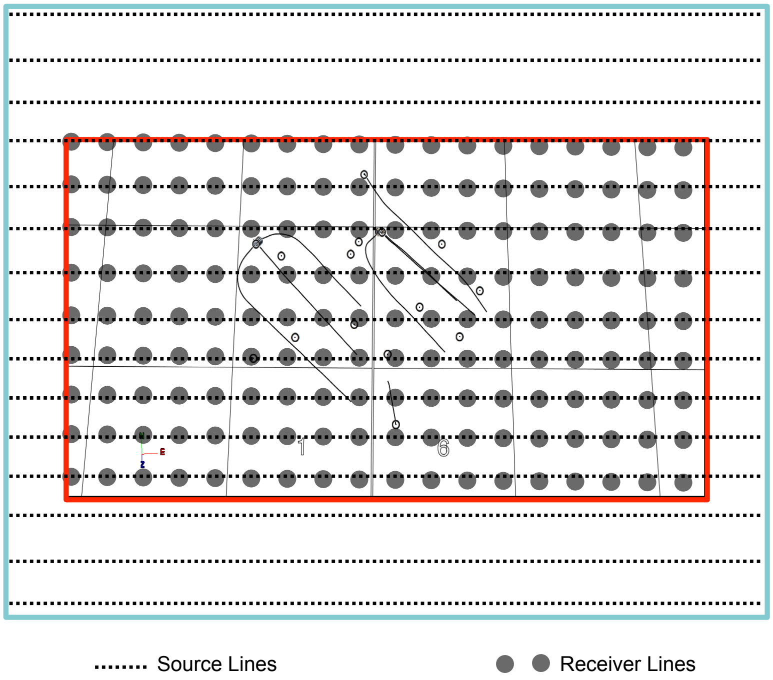

Figure 1.8: Pouce Coupe time-lapse, multicomponent seismic survey acquisition layout. Resulting 5 km^2 patch centered over horizontal wells 2-07 and 7-07. Modified from Atkinson (2010).

The acquired time-lapse, multicomponent seismic data from the given parameters results in a high fold (~ 70 fold at reservoir level) and full azimuthal coverage (360^0), required for time-lapse anisotropy measurements.

1.4.2 Microseismic Data

Microseismic data were acquired to passively monitor the hydraulic fracture energy placement and propagation, through the detection of microseisms created by the "fracturing" of the reservoir. From the visualization of the character of microseisms, such event patterns as the fracture geometry (length, height, azimuth and asymmetry) and interaction with natural fractures and faults an estimate of the "stimulated reservoir volume" referring to the volume of fracture propagation, can be inferred.

Microseismic events must be related to the deformation response corresponding to shear failures (Cipolla et al., 2011). In competent rocks, these shear failures predominantly occur on pre-existing planes of weakness caused by natural fractures (Warpinski, 2009). Hydraulically induced fractures are expected to propagate parallel to the present day maximum horizontal stress orientation (regional S_{Hmax}) and vertically because S_V decreases upward. In the case of natural fracture interaction, the resulting structure of microseismic events are heavily dependent on the orientation of any natural fractures. As an example, if natural fractures are orientated orthogonal to S_{Hmax}, the hydraulic fracture interacts with these planes of weakness and causes a complex fracture network.

Three independent microseismic acquisition methods were used to passively monitor the hydraulic fracture treatments of the 2-07 and 7-07 horizontal wells. Surface microseismic acquired by Microseismic Inc., downhole microseismic by Pinnacle Technologies, and shallow water well microseismic by Apex HiPoint. Figure 1.10 and Figure 1.11 show the total microseismic solution corresponding to all three acquisition methods. Primary conclusions will be drawn from the vertical downhole 9-07-78-10W6 (referred to as the 9-07 well) single array microseismic solution because of the large number of recorded events (5706), high signal-to-noise ratio and the most consistent solutions.

The downhole microseismic data by Pinnacle Technologies were recorded from a 12-tool vertical array placed slightly above the target formation. The geometry of the observation allowed for accurate vertical growth imaging of both hydraulic stimulations. Due to a limited observation distance ($\sim$900 m as seen in Figure 1.9) caution must be exercised when interpreting the magnitude distribution of events occurring near the observation array as compared to the observation limit. Although the relative low number of events triggered during the 2-07 well stimulation may be interpreted as observation bias (Figure 1.12), when looking at the total solution (Figure 1.10), where no observation bias was expected the same lack of events were observed.

Event moment magnitudes observed were between -2 and -3.8 at distances between 160 m and 1100 m by the single array acquisition (Figure 1.13). With increased tool-event distance, the limit of magnitude detectability decreases; therefore, the 2-07 well stimulation events were detected down to a magnitude of only -3.2, which impose bias on energy density interpretation. The high moment magnitude events (-2.5 to -2) were triggered during the 7-07 well stimulation and occur mainly at the well toe.

Microseismic events occur out to the extent of the reservoir that is affected by the pressure front and do not directly correspond to the propped volume or effective stimulated volume contributing to production. Microseismic monitoring provides an additional method for fracture characterization and can help delineate zones of energy dissipation and opening of fractures.

Microseismic monitoring observation conclusions:

2-07 Well stimulation (5 stages):

- Dominant azimuth: complex trending N40^0E
- Fracture half-length: 120-140 m
- Fracture height growth: 90-150 m (most growth upward, stayed within Montney)

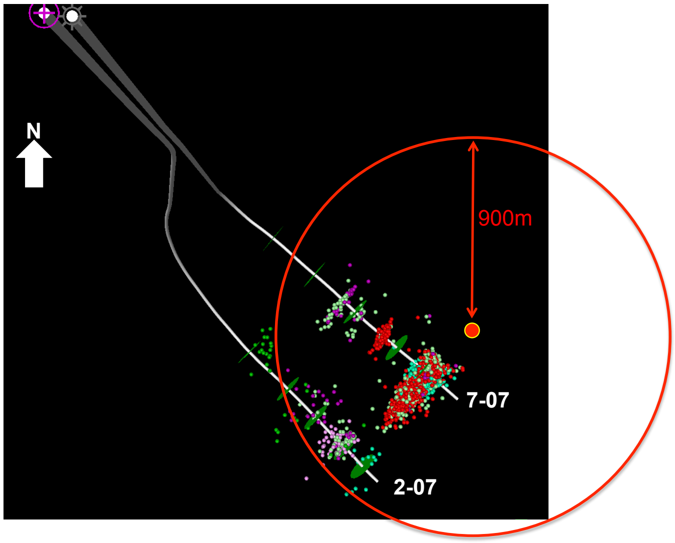

Figure 1.9: Map view of the vertical 9-07 well microseismic solution. An observation bias due to event detection limit is outlined by the red circle.

7-07 Well stimulation (5 stages):

- Dominant azimuth: N40^{0}E
- Fracture half-length: 260-370 m
- Fracture height growth: 100-250 m (most growth upward, stayed within Montney)
- Vast majority of microseismic events correspond to the Stage 1 (well toe)

1.4.3 Production Data

Production logs were run on both of the horizontal wells of interest (2-07 and 7-07 wells). Going beyond the conventional wellhead measurement of total production, this spinner log tool provides an estimation of fluid properties, pressures and flow rates for each stimulated stage. Stage-by-stage production can be used as a tool for quantifying the stage effectiveness and a method of correlating to the observed stimulation response.

ProTechnics of Core Lab used the Completion Profiler to collect the production profiling data. The Completion Profiler tool measures the velocity of the fluid with a spinner flow

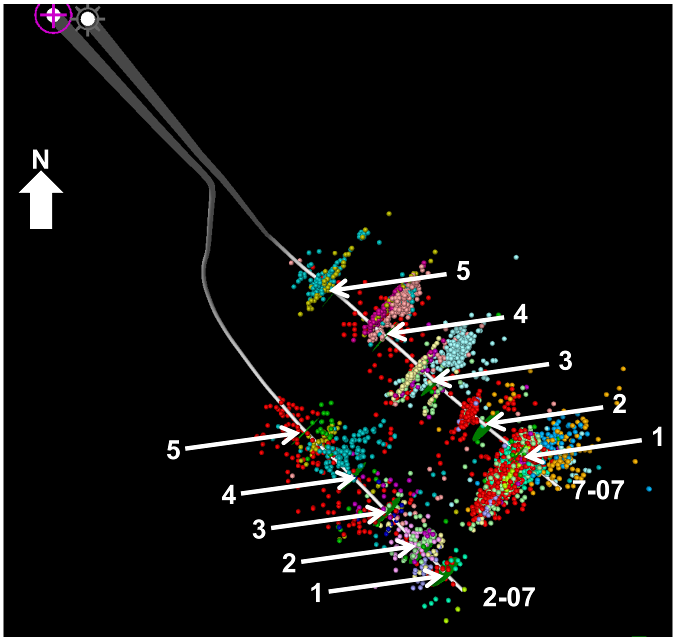

Figure 1.10: Map view of the total microseismic solution, all events from the three acquisition methods. Hydraulic fracture stage locations (perforation locations) labeled by an arrow and stage number.

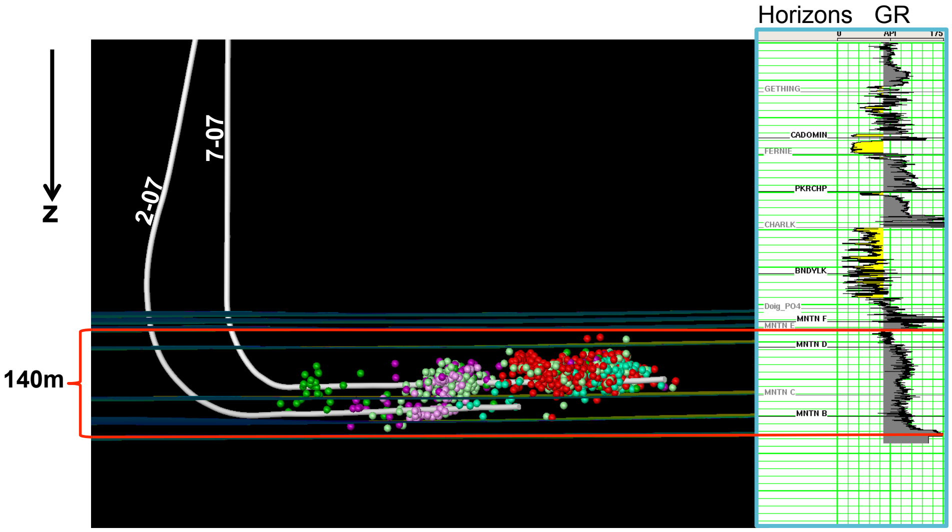

Figure 1.11: Microseismic profile, all events from the three acquisition methods.

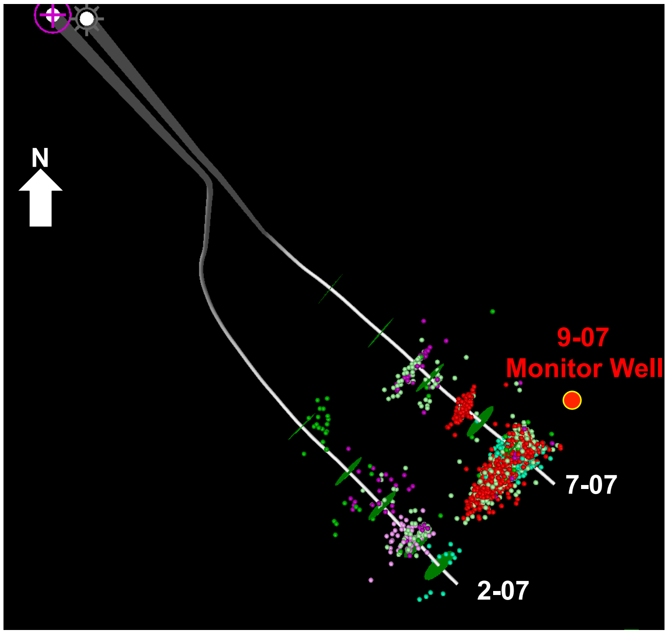

Figure 1.12: Microseismic events monitored from the vertical 9-07 well (location: red dot).

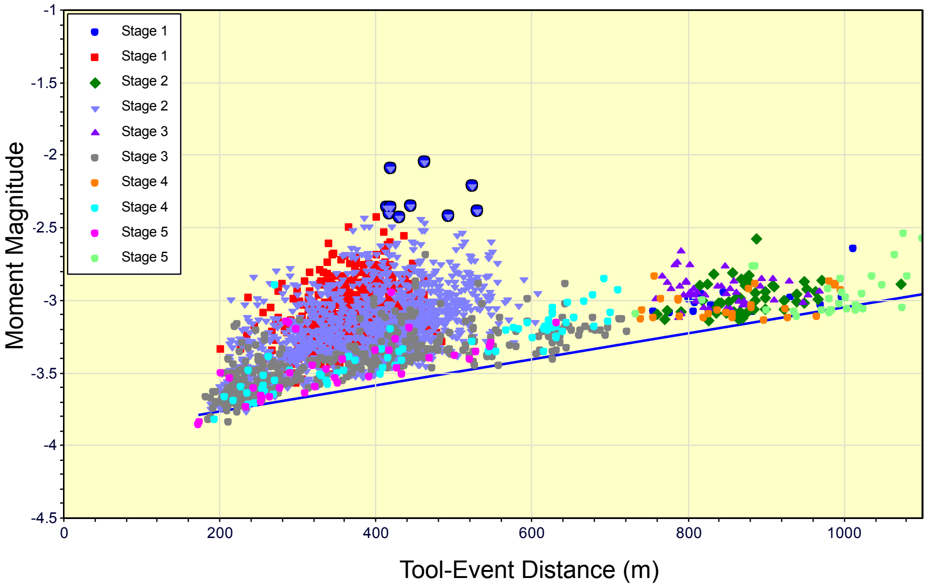

Figure 1.13: Event magnitudes vs. tool-event distance corresponding to the 9-07 single array solution.

meter. The fluid velocity is then converted to a flow rate (m^3/d). As the tool is pulled from the toe to the heel of the wellbore, it measures the total flow, which at any point represents the integrated flow below the measurement location.

The spinner data were collected January 13, 2009 (2-07 well) and January 15, 2009 (7-07 well), a month after hydraulic stimulation of each well. The measurements and interpretation are based on a finite time interval and may not accurately depict the absolute effectiveness of each stimulation stage Though some areas of the Montney are more liquid rich, in this area condensate contributes less than 0.04% and water less then 1.6%. This small contribution of liquids was insignificant; therefore, the gas production only was used to reflect the overall production and the overall fluid content within the reservoir. For this analysis, the spinner production data will be assumed to accurately reflect the stimulation effectiveness.

The production profiles for each well are shown in Figure 1.14, and Figure 1.15. The production was broken down by stage and given as a percent of total gas flow (Stage 1 referring to the toe or end of the wellbore). The log run on the 2-07 well could not reach the bottom of the wellbore, therefore Stage 2 shows the contribution from both Stage 1 and 2 (Figure 1.14). From the production profile it is easy to see that Stage 3 contributes the majority of the total flow (43%) and Stages 1 and 2 contribute 32% of the total flow. The production profile for the 7-07 well shows a much more uniform flow contribution from each stage (Figure 1.15). Stage 1 only contributed 6% of the flow and was anomalously low.

Total production numbers were also collected at the wellhead to compare the overall well effectiveness. Comparing the total flow, which is a summation of the contribution of all stages, by volume the 2-07 well produced 39% more gas than the 7-07 well. The difference in production will be examined further based on stimulation effectiveness.

1.5 Geomechanical Observations

To relate my work to the borehole scale, results from a geomechanical study undertaken by my colleague Heather Davey will be outlined here. Analyzing geomechanical rock

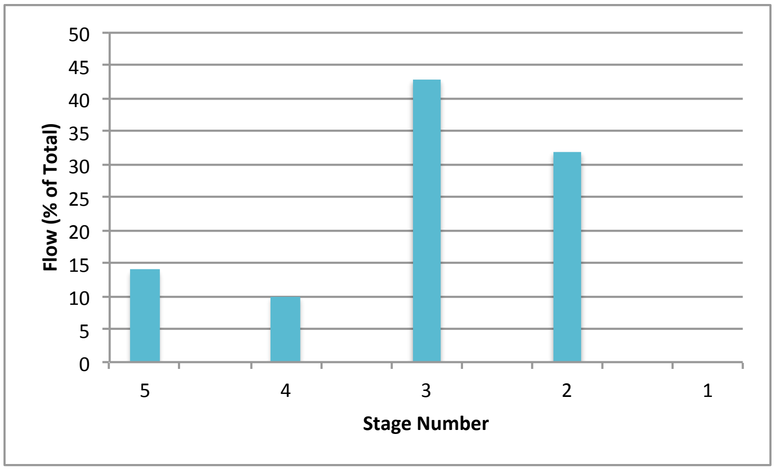

Figure 1.14: 2-07 well stage-by-stage production data.

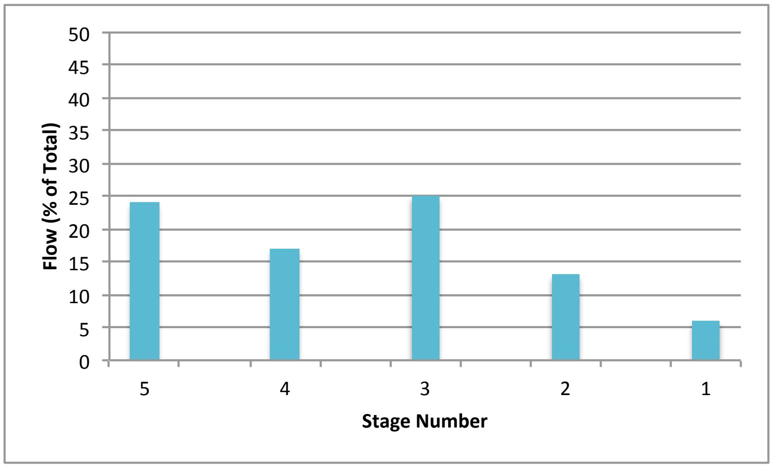

Figure 1.15: 7-07 well stage-by-stage production data.

properties at the borehole scale allows for hypotheses to be made regarding the behavior of microseismic and time-lapse multicomponent seismic monitoring. Geomechanical hypotheses are particularly important in tight reservoirs where hydraulic stimulations are required to create secondary permeability pathways and modelled stimulation responses are highly variable.

The mechanical stratigraphy, fracture characteristics, and stress state determine the vertical and lateral variations in stimulation response within a shale formation. Variations in stimulation response are related to burial history, compaction, hydrocarbon generation and phase, diagenesis, tectonic history, fracture character and the present day in-situ stress state (Davey, 2012). These factors can be classified under two explicit categories: compositional variation and fabric variation (Davey, 2012). The dependence of stress anisotropy, fracturing, and rock properties on the rock's composition and fabric is examined through the derivation of a Rock Quality Index (RQI), formulated by Heather Davey. Differences in these factors (both vertically and laterally) are heterogeneities that are dependent on mechanical properties caused by the depositional environment and stratigraphic framework.

Geomechanical properties of a reservoir are typically analyzed during the field development phase, creating a lag between drilling and best resource recovery practices. Creating a geomechanical model during the exploration phase can help characterize the reservoir and determine if the reservoir is economically viable to produce. Early understanding of the geomechanical framework allows for delineation of areas of best reservoir quality, optimal well azimuth, and differential stimulation design.

Following the pre-drill exploration phase, investigating the changes in geomechanical properties caused during drilling and hydraulic stimulation, as well as during production and depletion of the reservoir, are critical to long-term field scale resource development. In this study, my focus was on the integration of time-lapse multicomponent seismic analysis, microseismic monitoring, and geomechanics. Due to the lack of geomechanical data in the Pouce Coupe Field, many of the conclusions are formed in Farrell Creek Field (an adjacent

Montney field) and correlated to observations within the seismic study area. For a more detailed analysis of the geomechanics and well log scale details please see Davey (2012).

1.5.1 Geomechanical Model

Geomechanical modeling focuses on analyzing how stress deforms and breaks rock, and the influence of rock properties on production “sweet spots”. A geomechanical model consists of the mechanical stratigraphy, rock quality, stress state, and fracture analysis, allowing the prediction of how the reservoir will react to drilling, stimulation and production.

The rock property framework is generated through well log-based mechanical stratigraphy to determine property variations and complexities. Stress state and the principal stress orientations are derived from reservoir stimulation tests, image log analysis of drilling induced fractures and borehole breakouts. Using image logs, the natural fracture azimuth and dip are determined. Building on the determined reservoir properties and natural fracture characteristics the hydraulic fracturing is examined.

1.5.2 Stress

As stated above, the stress conditions are critical in determining the mechanical behavior of the reservoir. Stress state controls the existence of natural fractures, the type of fracture slip, the direction of induced fracture propagation and the optimal-drilling azimuth (wellbore stability and ease of drilling). Therefore, the vital stress parameters to be determined are: the magnitudes of the principal stresses (stress ratios) and orientations.

The regional stress regime within the Pouce Coupe Field is characterized as strike-slip (Davey, 2012), meaning that the overburden stress (S_V) is the medial stress and the two horizontal principal stresses represent the maximum and minimum stress magnitudes (S_{Hmax} and S_{hmin}, respectively) Figure 1.16. The overburden stress is determined by integrating the density from the surface to the top of the reservoir. The horizontal stresses are derived from drilling reports and minifrac tests to determine the pore pressure and stress components.

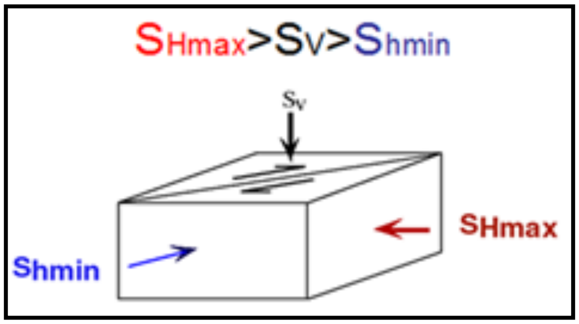

Figure 1.16: Strike slip stress regime model representing the regional in-situ principal stresses of the Pouce Coupe Field.

Within the Pouce Coupe Field, the regional maximum horizontal stress orientation is approximated to be N40^{0}E (Figure 1.6). The variations from the regional maximum horizontal stress direction are typical of the Peace River Arch and can easily be inferred from microseismic data and the deviation from the bi-wing hydraulic fracture model.

1.5.3 Mechanical Stratigraphy

Mechanical stratigraphy defines the fundamental relationship between stratigraphic cycles and the corresponding rock property variations. The definition of mechanical stratigraphy is directly related to the lithology (stratigraphic position and mineralogy), pressure and temperature conditions (thermal maturity) and the strain history (stress and natural fracturing).

The mechanical stratigraphy is interpreted using a standard suite of well logs, rock properties, and the Rock Quality Index (described in the next section) (Figure 1.17). The gamma ray, density, and sonic logs are used in conjunction with the Young's Modulus and Brittleness Index to define rock types in the reservoir. The result is correlated sections of relative brittleness, relative ductility and laminated/condensed characteristics.

Relatively brittle zones correspond to facies with a greater proportion of silica, meaning the rock is expected to break more easily and fractures will propagate further. The relatively ductile sections are characteristic of lower quartz content and lower Young's Modulus and

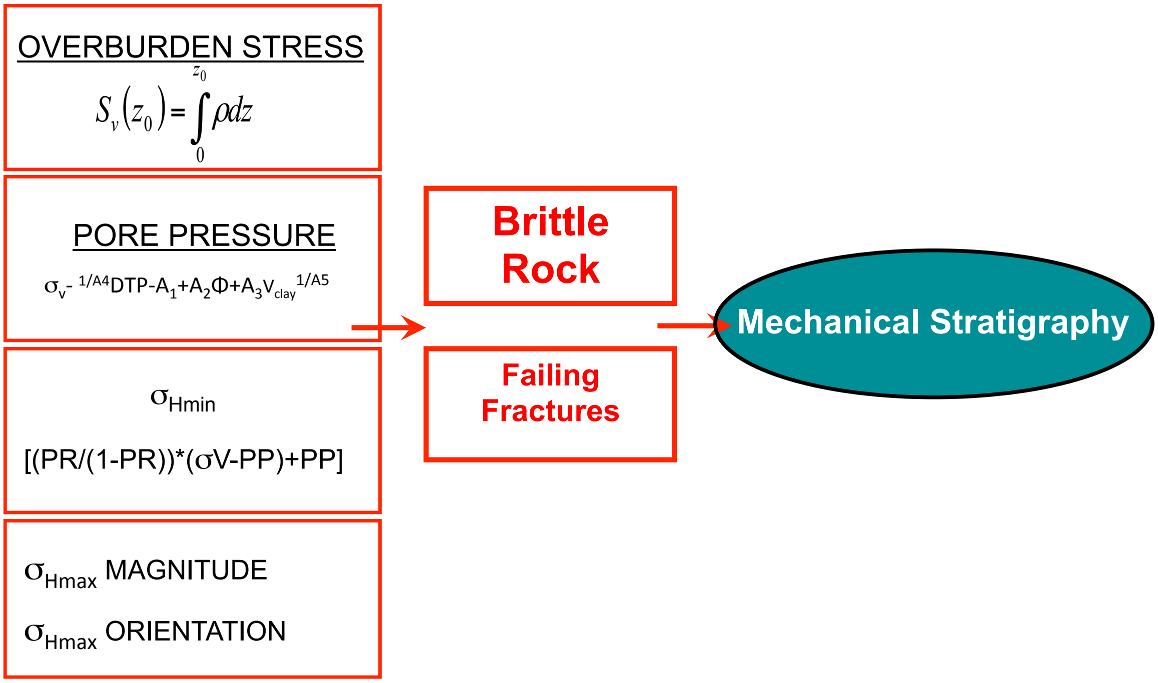

Figure 1.17: Geomechanical inputs and flow for the mechanical stratigraphy definition to determine brittle zones and failure failure (Davey, 2012).

are not expected to fracture. Condensed sections within the Montney reservoir act as shear failure zones and vertical propagation barriers to a hydraulic fracture; therefore resulting in less height growth within the formation (Davey, 2012).

For this project the mechanical stratigraphic framework was first derived in the Farrell Creek Field Montney location because of a wealth of log data and then slightly modified to characterize the Pouce Coupe Field properties (Figure 1.18). Depositional character of Pouce Coupe Field is different then Farrell Creek Field due to the change in stratigraphic setting to a position further up the slope and the resulting absence of condensed sections (Davey, 2012).

1.5.4 Rock Quality Index

To further expand on the mechanical stratigraphy definition, Heather Davey modified the Rock Quality Index (RQI) parameter. The formula attempts to delineates zones of brittleness or better hydraulic fracture propagation.

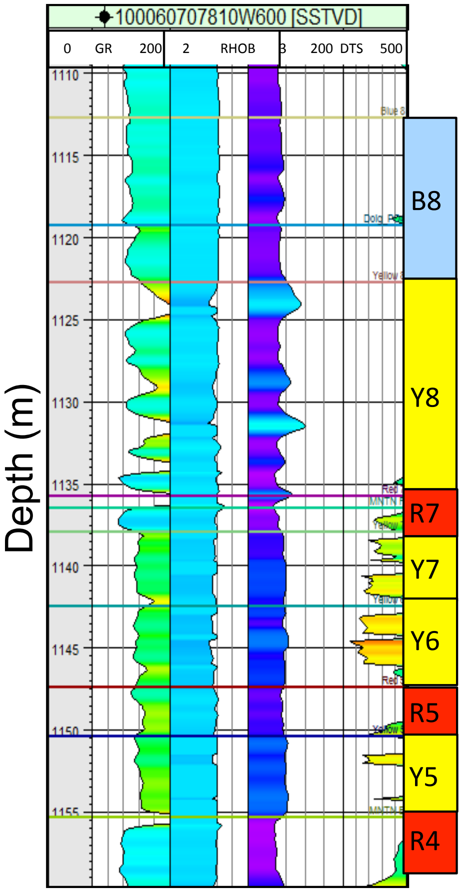

Figure 1.18: Pouce Coupe Field Montney mechanical stratigraphy defined by (Davey, 2012).Yellow facies are relatively ductile, red facies are relatively brittle, and blue facies are relatively laminated/brittle.

The formulation is based on three criteria: depositional conditions (rock fabric), petrographic conditions (rock composition), and differential stress ratio (rock physics model) (Figure 1.19). Formation brittleness and the corresponding RQI were found to be heavily dependent on heterogeneities within the formation, due to factors such as TOC content, porosity, laminations, and rock property changes (Davey, 2012).

Figure 1.20 shows the calculated RQI for the horizontal portion of the 7-07 well. The calculated RQI varies along the well bore, changing slowly in some zones and exhibiting quick variations in other zones. Zones of slowly varying RQI are hypothesized to allow for hydraulic energy to propagate more easily, and as this energy reaches a brittle zone, widespread fracture failure and extensive energy dissipation would be observed (Davey, 2012). From the calculated RQI, two zones of high values are identifiable, one at the toe of the well (stages 1 and 2) and another between Stage 3 and 4, outlined in red (Figure 1.20). Near stages 2 and 3, the calculated RQI varies more slowly and deemed a more homogenous zone.

For a full explanation of the definition and interpretation of the RQI please see Davey (2012).

1.5.5 Natural Fractures

Natural fractures are critical in the overall stimulation and production of shale reservoirs. As well as being planes of weakness during stimulation, natural fractures are potentially important in enhancing the reservoir permeability pathways. Natural fractures are related to rock evolution, zones of higher brittleness and provide a predictive tool for future fracture behavior in the present day stratigraphy and stress state (Davey, 2012).

In-situ fracture characterization through image logs is widely used in the industry. From the image logs analysis, the orientation, dip, aperture and density can be determined. Within the Pouce Coupe Field no image logs were acquired; therefore, analyses of the fracture orientation and dip from the Farrell Creek Field were used to approximate fracture properties in the Pouce Coupe Field. The use of seismically derived orientations and density (discussed

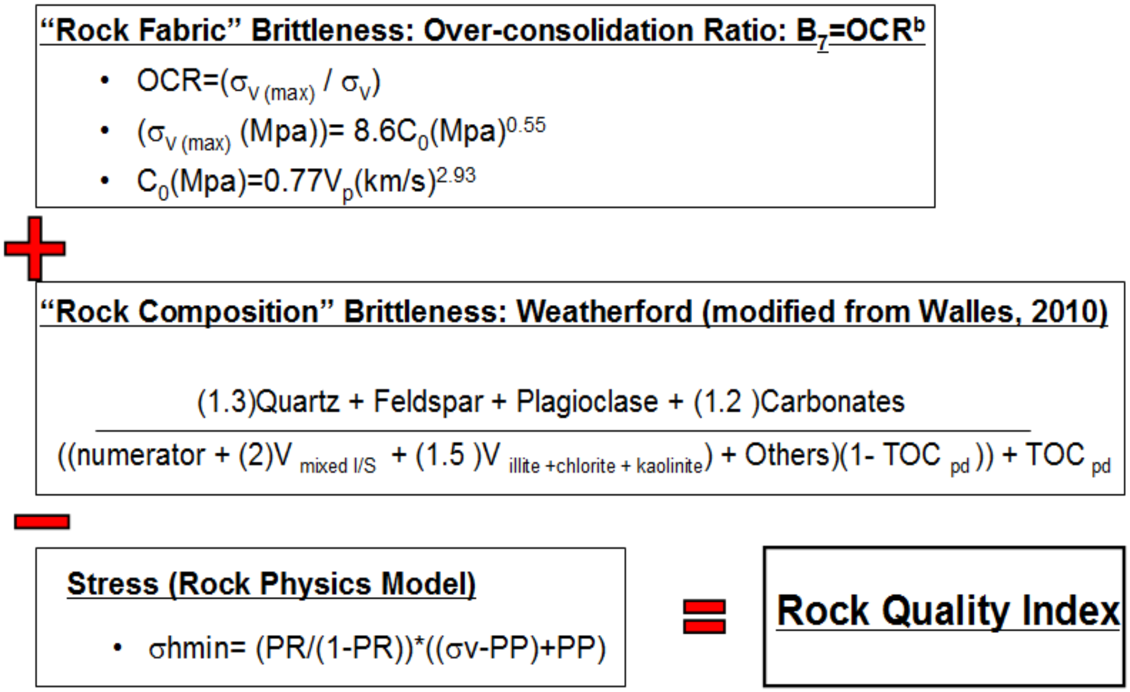

"Rock Fabric" Brittleness: Over-consolidation Ratio: B_7=OCR^b

- OCR=($\sigma_{V\,(max)}$ / σ_V)
- ($\sigma_{V\,(max)}$ (Mpa))= 8.6C_0(Mpa)$^{0.55}$
- C_0(Mpa)=0.77V_p(km/s)$^{2.93}$

+

"Rock Composition" Brittleness: Weatherford (modified from Walles, 2010)

$$\frac{(1.3)\text{Quartz} + \text{Feldspar} + \text{Plagioclase} + (1.2)\text{Carbonates}}{((\text{numerator} + (2)V_{\text{mixed I/S}} + (1.5)V_{\text{illite + chlorite + kaolinite}}) + \text{Others})(1 - \text{TOC}_{pd})) + \text{TOC}_{pd}}$$

−

Stress (Rock Physics Model)

- σhmin= (PR/(1-PR))*((σv-PP)+PP)

=

Rock Quality Index

Figure 1.19: Parameters for the RQI formulation. Rock fabric and rock composition-based brittleness terms are added together, and then minimum horizontal stress is subtracted to generate the RQI (Davey, 2012).

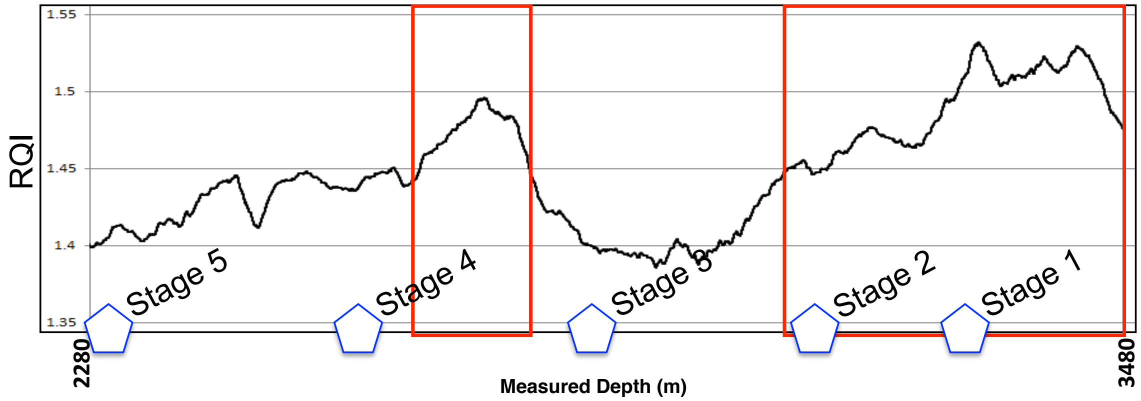

Figure 1.20: Calculated RQI for the horizontal 7-07 well (Davey, 2012).

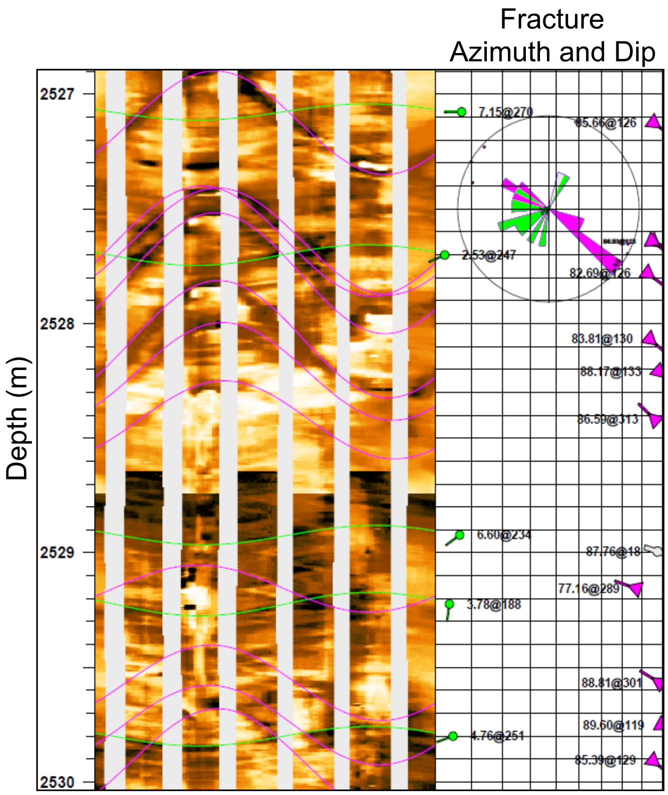

Figure 1.21: Farrell Creek Field image log example within the Montney reservoir interval. Case of near vertical natural fractures with consistent orientation (purple) (Davey, 2012).

in Chapter 4) were then compared to the image log analysis at Farrell Creek Field.

From image log analysis in the Farrell Creek Field (Figure 1.21), it was determined that each wellbore contained two natural fracture orientations; one roughly parallel to the regional S_{Hmax} (N40^0E) and the other roughly orthogonal to it (Davey, 2012). In general, approximately 65% of total wellbore fractures were found to strike in one of these two orientations; however, the dominant fracture orientation varied from well to well over the field area (Davey, 2012).

The two sets of fractures were both interpreted to be steeply dipping ($\sim 80^0$), which is crucial for the seismic imaging of fractures systems and provided confidence in the use of shear-wave splitting analysis as a correlation tool for the borehole scale fracture conclusions (results and interpretation in Chapter 4).

1.5.6 Fracture Failure

The overall stimulation success of a shale reservoir relies on both induced hydraulic fractures and natural fractures and is therefore inherently complex. It is observed that certain orientations of natural fractures within the Montney reservoir have a tendency to fail first with an increase in pore pressure (as seen through Mohr-Coulomb failure analysis in Figure 1.22).

Mohr-Coulomb failure theory was used to examine effective stress changes due to hydraulic fracture stimulations. Examining the Terzaghis equation (Equation 1.1), an increase in the pore pressure (PP) there is a reduction in effective stress (S_{eff}) and the stress state shifts to the left (blue circle) causing any fracture lying on the portion of the semi-circle which surpasses the shear failure envelope to be critically-stressed and fail in shear (Figure 1.22).

$$S_{eff} = S_V - \alpha PP \tag{1.1}$$

Here, S_V is the overburden stress; integration of density from the surface to target depth and α represents the Biot coefficient typically equal to 1.

It was concluded that fractures orientated in relation to the highest fracture density were failing first. In some instances fracture failure occurred in orientations roughly parallel to the direction of the regional average minimum horizontal stress (N50^0W) (Davey, 2012). Possible reasons for this type of fracture failure progression can be seen in the analysis by Heather Davey, however, it is assumed that hydraulic fracture dilation against orthogonal natural fractures sets creates high compressive stress, which translates into shear movement along the fracture plane. When this type of interaction occurred (i.e. where wellbores contained fractures dominantly aligned with S_{hmin}), higher 200 day production rates were observed (Davey, 2012).

In an isotropic reservoir without any natural fractures, the propagation direction of hydraulic fractures is strictly dependent on the anisotropic stress orientation and magnitudes.

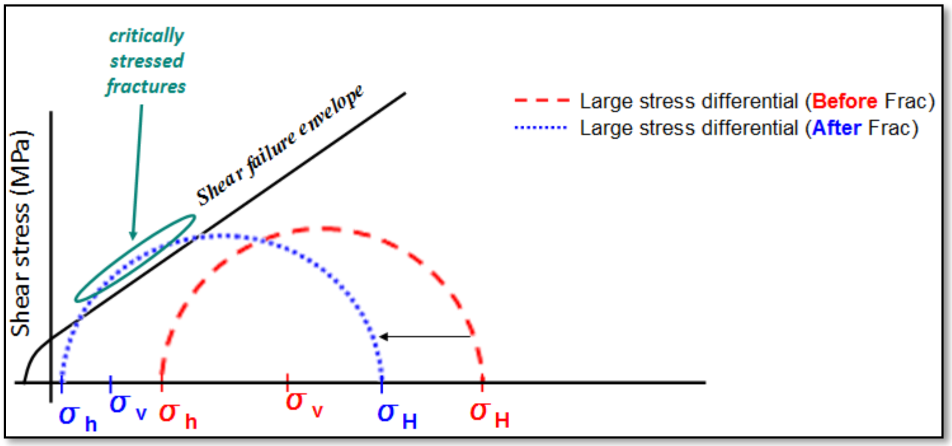

Figure 1.22: Mohr-Coulomb failure theory. With an increase in pore pressure there is an overall reduction in effective stress and the stress state shifts to the left (blue), from the original in-situ reservoir state (red circle). Any fracture lying on the portion of the semi-circle (blue) surpass the shear failure envelope will be critically-stressed, causing shear failure. (Davey, 2012).

The expectation is that in the strike-slip stress regime characteristic of Pouce Coupe Field hydraulic fractures will favorably propagate in the S_{Hmax} orientation and therefore, we would not expect high vertical fracture growth.

Given that a hydraulic fracture preferentially propagates parallel to the maximum horizontal stress direction, if there is a natural fracture system orthogonal to this, then a complex (connected) fracture network development would be expected (Figure 1.23). The case of natural fractures parallel to the regional maximum horizontal stress direction, less complexity of the fracture network would be expected, but fractures would likely be connected to the wellbore, and deemed an effective network of fracture permeability.

1.5.7 Geomechanical Conclusion

Geomechanics was used to hypothesize how formation properties will influence hydraulic fracture stimulations. From Davey (2012) it was concluded that the stress magnitudes and orientations, rock quality and natural fractures were governing factors for explaining differences in hydraulic stimulation effectiveness.

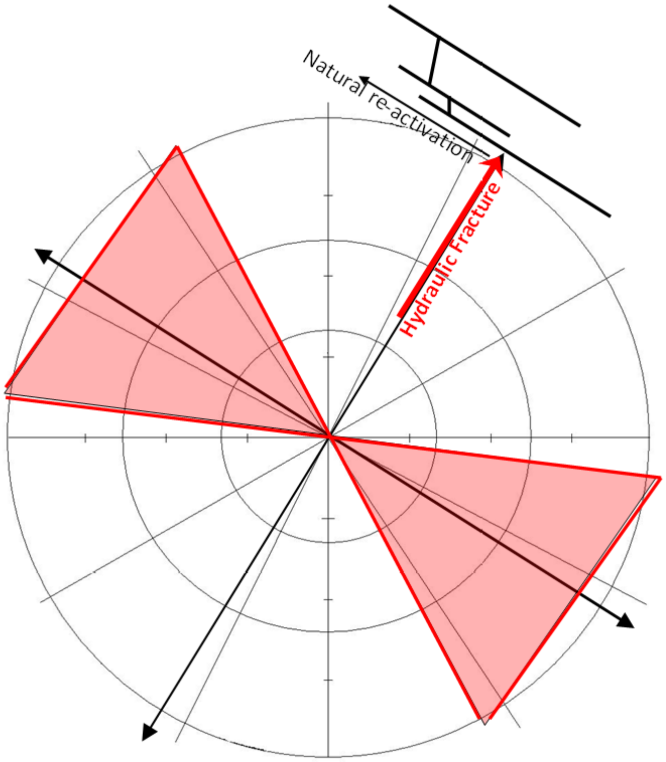

Figure 1.23: Fracture failure model for abundance of natural fractures orientated orthogonal to S_{Hmax} (N40^0E). The hydraulic fracture will propagate in the S_{Hmax} direction (shown by red arrow) encountering the natural fracture set, causing fracture orthogonal re-activation (Davey, 2012).

A modified version of the Rock Quantity Index (RQI) parameter determines production "sweet spots" suggesting rock brittleness or hydraulic "fracability" parameterized by mineralogy, mechanical properties and stresses within the reservoir interval. The regional stress regime within the Pouce Coupe Field was characterized as strike-slip, with a regional average S_{Hmax} oriented N40^{0}E. Within the Montney reservoir, two roughly orthogonal natural fracture sets are present, one roughly parallel to the regional S_{Hmax} and an orthogonal set. From Mohr-Coulomb analysis it was determined that in some instances the fractures failing first were those occurring in orientations approximately orthogonal to S_{Hmax}. The inherent weakness planes associated with the dominant natural fracture orientation determine the propagation of hydraulic energy. A complex fracture network would be expected due to the hydraulic and natural fracture interaction.

1.6 Previous Work

Atkinson (2010) showed that the Pouce Coupe time-lapse multicomponent seismic data set could image the hydraulic fracturing effects. An initial hypothesis proposed that compressional-wave (P-wave) monitoring of hydraulic fracturing would respond to an expected pore pressure increase. Through modeling and seismic analysis preformed by Atkinson (2010) of the time-lapse compressional wave data, the volume of rock experiencing the increase in pore pressure was determined too insignificant to be monitored, counter to more conventional permeable reservoirs. However, utilizing converted-wave data, anisotropy was deemed distinguishable in time delays between the fast and slow converted-waves (PS_1- and PS_2-wave, respectively) corresponding to the shear-wave splitting.

The presence of fractures, within the Montney reservoir, both natural and hydraulically induced, was concluded to show an expected shear-wave splitting response in the converted-wave seismic data (Figure 1.24 and Figure 1.25). The method used to measure the shear-wave splitting by Atkinson (2010) was to sum the negative time-variant time-shifts over the reservoir time window. Although the seismic volumes showed a shear-wave splitting response, the layer stripping and non-repeatable noise still imposed some erroneous imprint on the time-lapse analysis.

The processing performed in the Atkinson (2010) study included layer-stripped the overburden as a whole by estimating one average orientation and the bulk time delay removal. The method of layer stripping used in this previous study was assumed to reduce any significant overburden anisotropy but not completely remove it. From the results produced by Atkinson (2010), the time-shifts in the overburden still had some imprint at the reservoir level and had to be accounted for in the interpretation.

The converted-wave data were sufficient in monitoring the response caused by induced-hydraulic fracturing but concluded that additional advancements in the processing of time-lapse, multicomponent data were required. Additionally, it was recommended that production information be integrated with microseismic and shear-wave splitting to interpret the hydraulic stimulation response and associated stimulated volume.

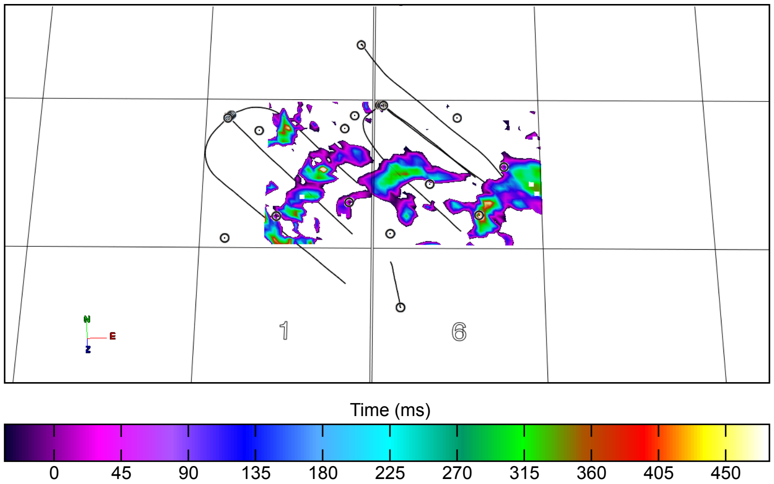

Figure 1.24: Shear-wave splitting time delays (Monitor 1 minus Baseline) calculated by Atkinson (2010).

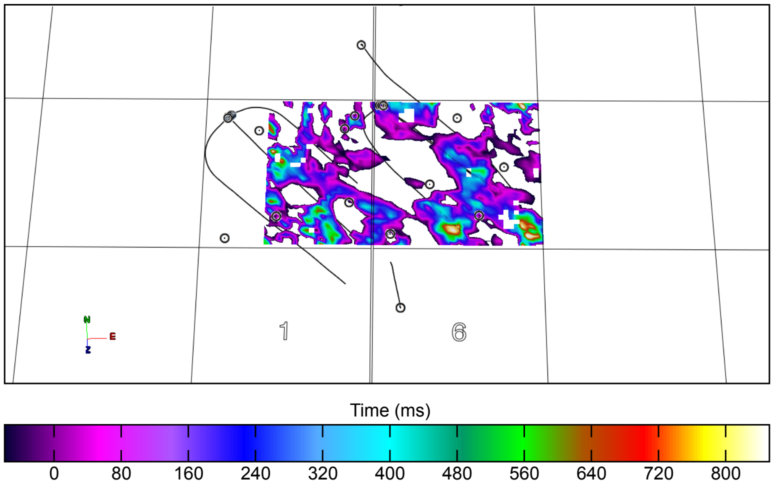

Figure 1.25: Shear-wave splitting time delays (Monitor 2 minus Monitor 1) calculated by Atkinson (2010).

CHAPTER 2

TIME-LAPSE, MULTICOMPONENT SEISMIC DATA PROCESSING

2.1 Introduction

In this chapter the time-lapse, multicomponent seismic processing flow and theory will be outlined. Sensor Geophysical, focusing on the final interpretation goals of fracture characterization and hydraulic fracture monitoring, reprocessed the Pouce Coupe 4D-3C seismic survey. The reprocessing improved over previous processing results (Atkinson and Davis, 2011) by deploying new methods to better preserve vector fidelity, enhance time-lapse repeatability, and improved prestack shear-wave splitting analysis for layer stripping.

Land multicomponent processing has made significant improvements within recent years due to the application of more sophisticated algorithms and proper pretreatment of the data. Proper handling of multicomponent data requires careful handling of the wave-fields, geometries, polarities and surface statics.

To address vector fidelity problems of the recorded converted-waves associated with receiver/geophone misorientation, a method for automatically detecting and correcting receiver azimuths called Receiver Azimuth Detection and Rotation (RADAR) was utilized. This pretreatment of the data greatly improved the quality of the subsequent steps of processing the horizontal receiver components.

To accurately image the reservoir properties, layer stripping was performed on the overburden to rid the anisotropy effects while preserving meaningful anisotropy variations at the reservoir level. The layer stripping algorithm implemented on the Pouce Coupe seismic data differs from conventional methodology by using the maximum stacking power of the radial component instead of minimizing the energy in the transverse component; this allows for improvement in low anisotropy conditions.

Multicomponent data processing is only one part of the processing sequence. Since this survey is composed of multiple seismic surveys, the data must also be treated to maximize the repeatability. Because the acquisition geometry was kept constant using permanent sensors and cased shot holes, the non-repeatable noise is attributed to changes in the near surface conditions, field operation noise and source/receiver coupling issues. Minimizing the difference between the baseline and monitors surveys is achieved by simultaneously processing all volumes as one data set. Sensor Geophysical accomplished this by combining the three Pouce Coupe seismic surveys into a super set of data and then treated as one survey. Each processing step is quality checked to ensure an increase in the repeatability characterized by lowering the normalized root mean square (NRMS) value (Li et al., 2011).

The main steps of multicomponent processing are outlined (Table 2.1) and improvements to the processing sequence and algorithms are discussed in further detail.

2.2 Converted-wave Data

A dynamite source generates a compressional-wave (P-wave) that travels downward through the subsurface and reflects off an impedance contrast producing a conventional upward traveling P-wave, referred to as a PP reflection. In anisotropic media, at this interface the P-wave converts to two S-waves traveling back to the surface receiver, these waves are referred to as a converted-waves (PS-waves) as seen in Figure 2.1. The velocity of the downgoing wavefield (P-wave) is not the same as the velocity of the upgoing wavefield (S-wave), and as a consequence common mid point principles no longer apply (Hardage et al., 2011). The asymmetry of the ray path is accounted for in the processing by assigning the correct image geometry.

Converted-wave data does not require a shear-source and therefore, the acquisition costs are lower then a 9-C survey (full shear). To record the PS-wave, three channel geophones are used and the horizontal components are used to determine the shear contributions to the received wavefield. Multicomponent acquisition requires careful field setup, three times the recording channels, and also much more detailed treatment of the data during the processing, making it a more extensive effort than conventional P-wave acquisition and processing. Still,

Table 2.1: Sensor Geophysical processing flow for the Pouce Coupe time-lapse, multicomponent seismic data.

Pouce Coupe Seismic Time-Lapse Multicomponent Processing Flow (July, 2012)	
Reformat	Record Length 6.0 seconds, Sample Interval 2ms
3D Geometry Assignment	Asymptotic Binning (50 x 50m)
RADAR	Geophone Orientation Analysis
H1/H2 Rotation	To Common Azimuth
H1/H2 to RAD/TRS Rotation	198.5 degrees
Sinusoidal Noise Removal	60Hz
Singular Value Decomposition	Ground Roll Removal
True Amplitude Recovery	Spherical Divergence (Corr.: Gain 8dB/s)
Surface-Consistent Deconvolution (Spiking)	Operator Length: 100ms Prewhitening: 0.1% Design Window: 100-3600ms at 45m offset 1300-4000ms at 3045m offset
Refraction Statics Correction (from PP)	Datum 900m Replacement Velocity: 2900m/s Processing Datum: Floating Layers Replaced: 2
Additional PS Receiver Statics	Derived from Common Receiver Stacks
Surface-Consistent Statics	Method: MASTT Correlation Maximum Shift: 20ms Correlation Window: 700-2000ms
Velocity Analysis	
Surface Consistent Amplitude Scaling	Shot/Reciever
T-F Adaptive Noise Suppression	
Offset Consistent Gain Control	
RAD/TRS LAS	0-360(10)degrees - PS_1/PS_2 Analysis
RAD/TRS Layer Stripping	3 Layers: 700-900ms 1000-1600ms 1700-2000ms
RAD/TRS to PS_1/PS_2 Rotation	PS_1/PS_2 Magnitude and Orientation
Velocity Analysis	
Surface Consistent Statics	Method: Stack Power Maximization Maximum Shift: 20ms Correlation Window: 700-2000ms
RAD/TRS Layer Stripping	Layer 4 Analysis 2150-2450ms
RAD/TRS to PS_1/PS_2 Rotation	PS_1/PS_2 Magnitude and Orientation
Normal Moveout Correction	Anisotropic: $\eta = 0.1$
Front-End Muting	Offset: 400, 700, 4500m Mute Time: 0, 600, 3100ms
3D Common Conversion Point Stack	$\gamma_{eff} = 55\%$ $+100ms$ Bulk Shift
F-XY Prediction Filtering	Operator Size: 3x3 Samples Time Window Length: 100ms Time Window Taper: 50ms
Anisotropic Diffusion Filter	Design Window: 5 traces x 11ms Number of Diffusion Steps: 1 Diffusion Rate: 0.25
Poststack Time Migration	Method: Implicit Finite Difference Dip Aperature: 0-65 degrees Velocity Function: 95% Smooth Stacking Velocities
Bandpass Filter	Zero-phase Ormsby: 10/15-40/50Hz

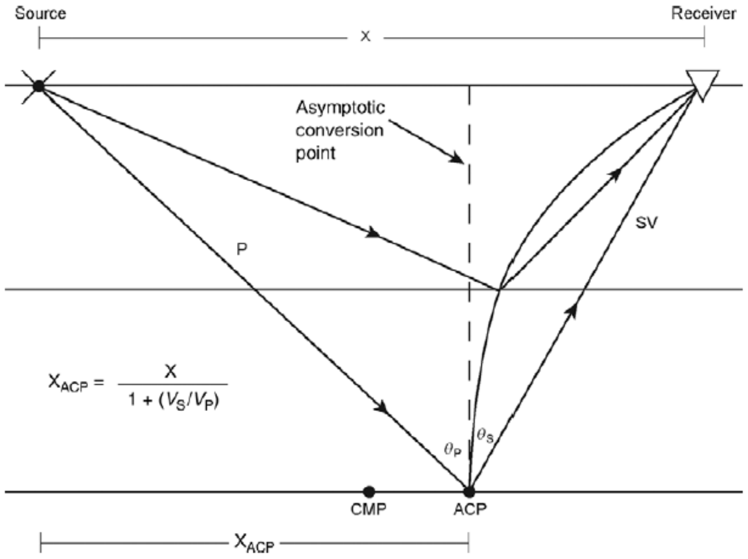

Figure 2.1: Typical converted-wave ray-path. Notice the asymmetry and the deviation from the asymptotic conversion point (ACP) of reflection (Hardage et al. (2011)).

the benefits of multicomponent data are proving to be worth the extra costs and time for certain situations.

There is an interest from the industry to use converted-waves for reservoir characterize. Conventional P-waves interpretation can fail to determine the fracture properties (Atkinson, 2010). Conversely, S-waves are highly sensitive to anisotropy caused by differential stress and preferentially orientated open fractures.

Converted-wave data have proven to improve the detection of faults (Davis and Benson, 2013), especially minimal offset wrench faults. Converted-waves are insensitive to fluid content and saturation conditions and exhibit little fluid bias when characterizing reservoir properties.

2.3 Receiver Azimuth Detection and Rotation

The data recorded on two horizontal components of the multicomponent receivers primarily represent the converted-waves and must be accurately orientated to properly characterize the correct signal. Orientations of the two horizontal components are typically assumed to

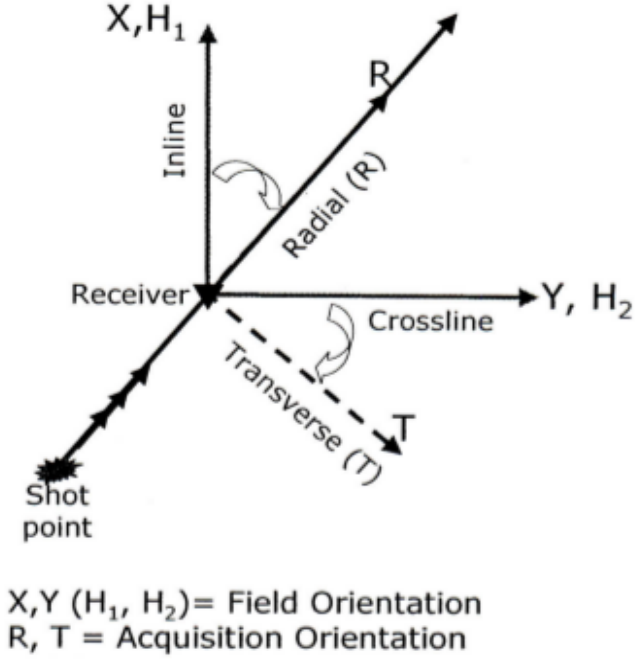

Figure 2.2: Field components $[H_1, H_2]$ and rotated receiver components [R,T].

be properly aligned to the inline and crossline directions, respectively (Figure 2.2). The coordinate system used for the field geometry requires the horizontal components $[H_1, H_2]$ to be rotated into orthogonal radial (source-to-receiver direction) and transverse coordinates [R,T] by a 2D Euler rotation, to properly process the converted-wave data (Grossman and Couzens, 2012). Errors in the orientation of the receivers can cause radial energy to be “leaked” onto the transverse component. This leaked energy or the existence of energy on the transverse component can easily be misinterpreted as shear-wave splitting (Cary, 2002). To correct for this vector infidelity, or energy-leakage problem, Sensor Geophysical recently developed high-fidelity algorithm for automatically detecting and correcting receiver azimuths developed called RADAR (receiver azimuth detection and rotation) (Grossman and Couzens, 2012). The RADAR algorithm was utilized on the Pouce Coupe time-lapse, multicomponent seismic data set.

To accurately determine the true field-set receiver orientation (or any deviations from the specified field report), the RADAR method based on the first recorded polarity is examined

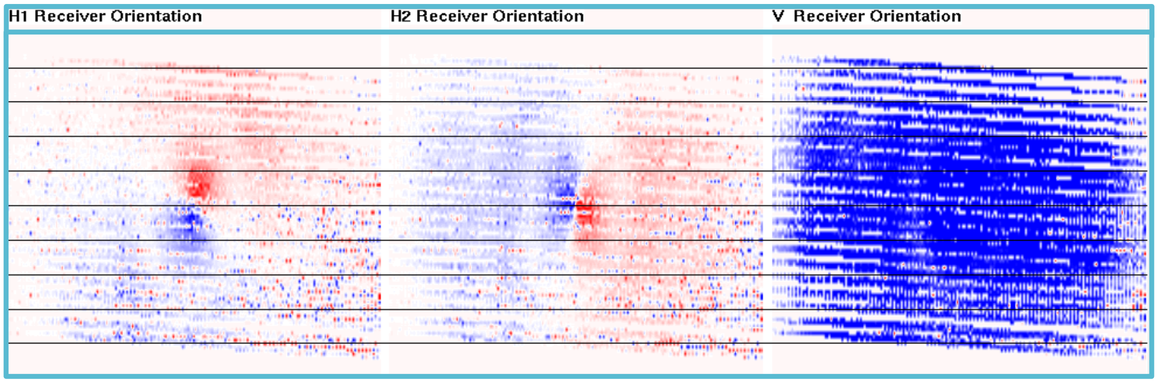

Figure 2.3: *P*-wave first break polarity maps for the three receiver components (RADAR). Modified from Sensor Geophysical.

for each receiver ensemble. The polarity was determined by measuring the *P*-wave first break (head-wave) amplitude from all shots at the receiver ensemble and performed on each of the recorded components. The *P*-wave polarity map represents all shots received at a central receiver location (Figure 2.3). For this receiver, the H1 component (X or inline component) is oriented at approximately 20^0 East, this is a good example of a properly orientated receiver conforming to the magnetic declination of Pouce Coupe Field, which was 19^0 East.

As a processing algorithm, RADAR was implemented for each receiver ensemble and the code constructs an objective function used to determine the best-fit azimuth. The first-break amplitude measure obtained in the previous step weights the contribution of each trace, and by scanning all trial azimuths the receivers orientation can be accurately determined. The final part of the process involves a global analysis of the results yielding a probability measure indicative of the confidence level associated with the receiver-azimuth estimate. If the function reaches a nontrivial solution associated with the global maxima, a reorientation is applied to the receiver ensemble (Grossman and Couzens, 2012).

Errors in receiver orientation are distinguished by anomalous azimuthal orientations (Figure 2.4). Orientation error was present at nearly 10% of the receivers and the amount of error ranged over all azimuths (-180 to 180 degrees).

The impact of this analysis on the Pouce Coupe converted-wave seismic data were il-

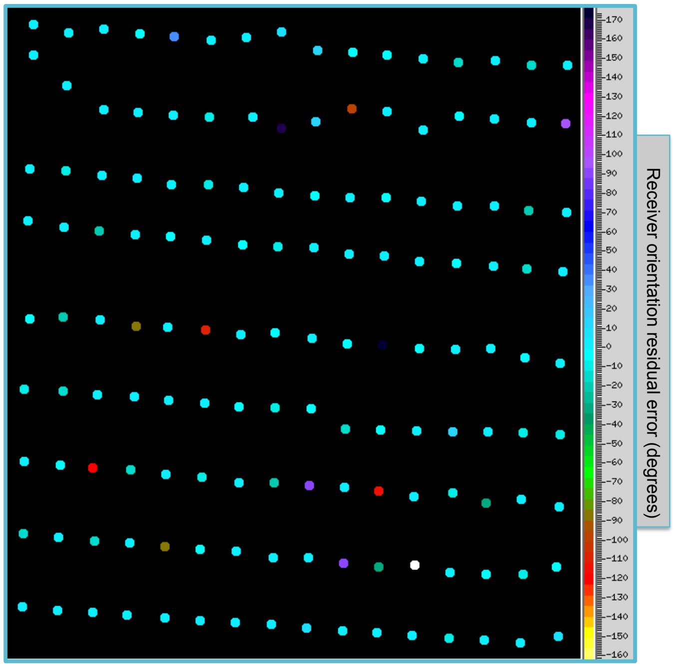

Figure 2.4: Receiver orientation estimates determined by first break energy polarities (RADAR).

lustrated by the increase in coherent energy on the radial receiver gather (Figure 2.5). In the original orientation receiver data (using field reports) the reflection events are incoherent, while coherent reflection events dominate the radial receiver gather after RADAR was applied. The result of correcting the receiver orientation significantly increases the signal-to-noise ratio and has many benefits in the subsequent processing steps.

2.4 Simultaneous Time-lapse Processing

The Pouce Coupe time-lapse multicomponent data set has been processed to achieve the highest possible repeatability between all three surveys. The repeatability between the surveys allows for any time-lapse effects to be interpreted as differences related only to changes in the reservoir properties (Landrø, 1999).

The repeatability between two input traces is quantified using the normalized root-mean-square (NRMS) error (Equation 2.1). Ideally, the NRMS error would go to zero but due to variations in receiver coupling and source fields, recorded seismic data are not 100%

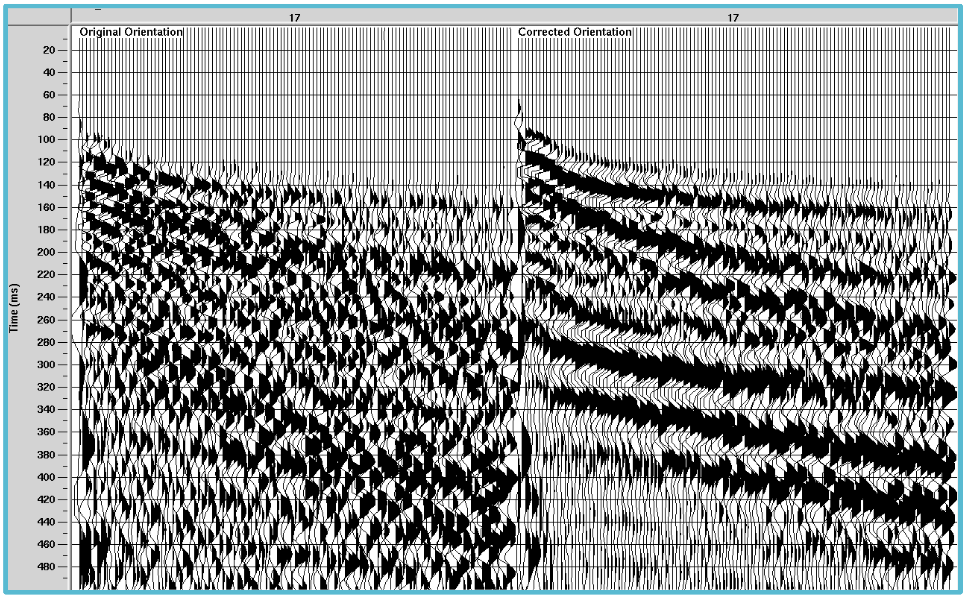

Figure 2.5: Radial receiver gathers, before and after RADAR has been applied.

repeatable. In the industry, repeatability is deemed acceptable when the NRMS error value is below 0.5.

$$NRMS(T_1, T_2) = \frac{2RMS(T_1 - T_2)}{RMS(T_1) + RMS(T_2)} \tag{2.1}$$

Maximum integrity of the time-lapse seismic data were achieved by simultaneously prestack processing the multiple seismic surveys (4D), while preserving meaningful information within the expected zone of change (Lumley, 2003). Simultaneous processing refers to the merging of multiple data sets into one super set of data; as seen in Figure 2.6, each channel represents a combination of the three vintages of traces, referred to as trace triplets.

Repeatability is maximized for reflection signal in the time window above the reservoir (red window in Figure 2.6) where time-lapse effects are not expected. After each key processing step, a quality control is performed both visually and quantitatively on the trace triplets and determined successful if the NRMS error value decreases (Li et al., 2011). The methodology of simultaneous processing also alleviates the need for further cross-equalizing the data after it has been stacked (Lumley, 2003). The full simultaneous processing methodology is

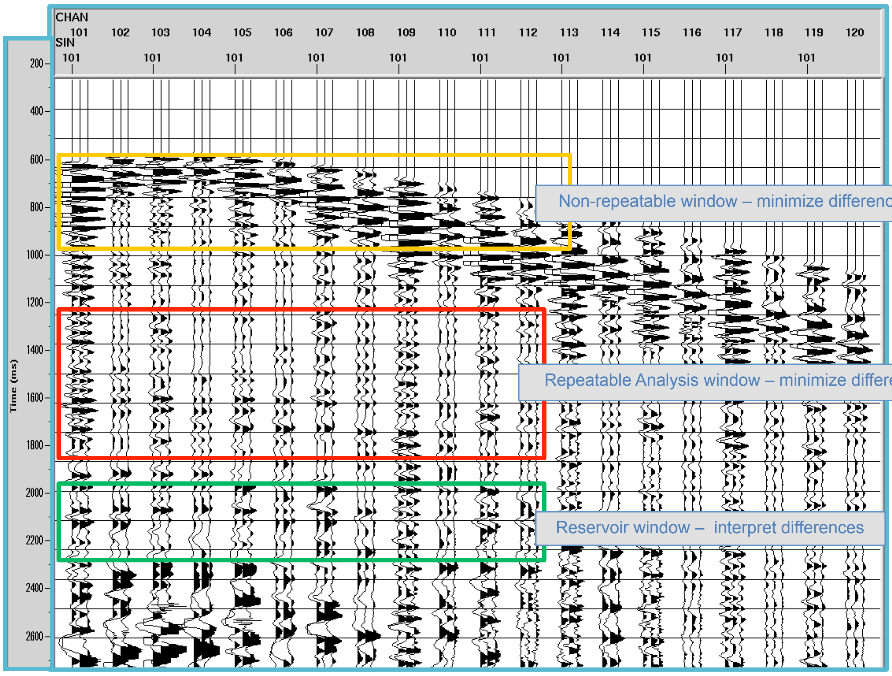

Figure 2.6: Trace triplets from raw data (each trace represents one vintage and combined at a single ACP location). The lack of repeatability is easily identified in the shapes of the wavelets and amplitude levels. Modified from Sensor Geophysical.

discussed in greater detail by (Li et al., 2011).

The NRMS error was found to decrease significantly over that of the previous processing (Figure 2.7). The improvements were attributed to the initial treatment of the receiver orientation pre-processing, the increase in signal-to-noise ratio and improved statics. Final result of simultaneously processing for maximum repeatability between Monitor 1 and Baseline and between Monitor 2 and Baseline are displayed respectively in Figure 2.8 and Figure 2.9.

Figure 2.8 and Figure 2.9 show great improvement in the lateral extent of the high repeatable area (<0.2 NRMS error) and the overall repeatability spectrum. The area outlined in Figure 2.8 corresponds to the high repeatability area and therefore the area of greatest confidence in the time-lapse anomalies. Interpretation is focused on this polygon area.

Simultaneous processing has shown to greatly improve the repeatability between these time-lapse multicomponent seismic surveys and has resulted in increased confidence in the interpretation of hydraulic fracture monitoring.

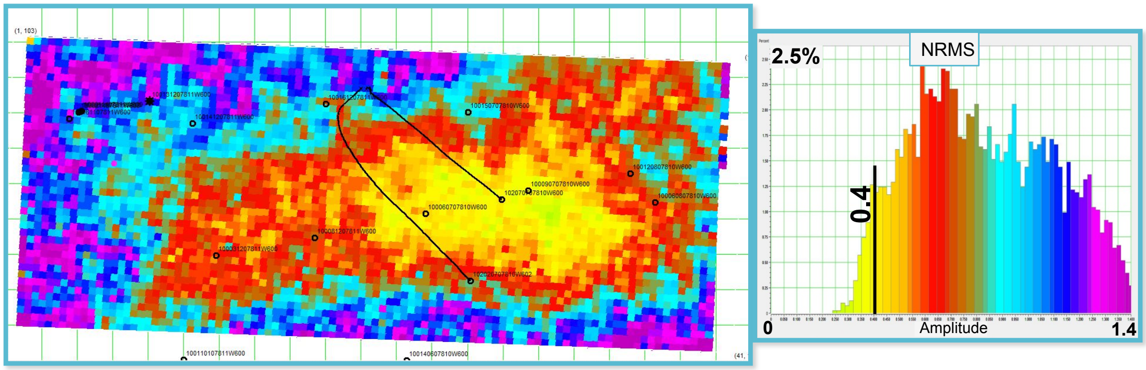

Figure 2.7: NRMS map and histogram from vintage processing.

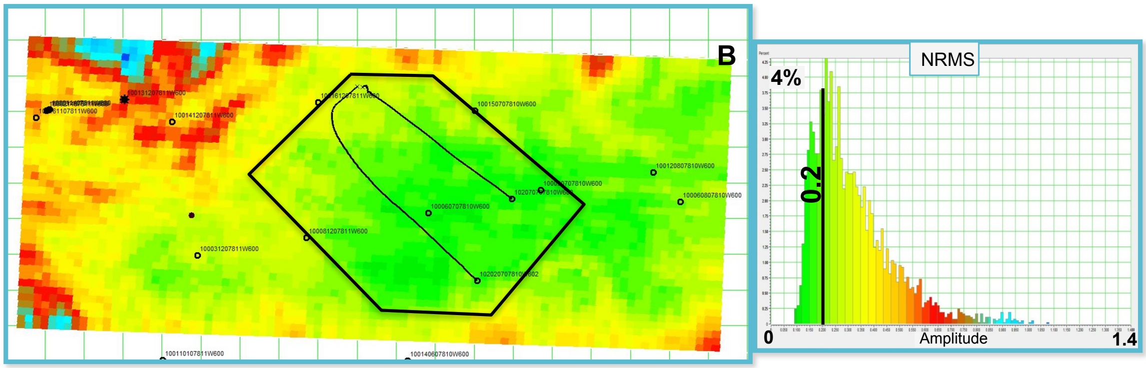

Figure 2.8: NRMS map and histogram for Monitor 1 minus Baseline (most recent processing results).

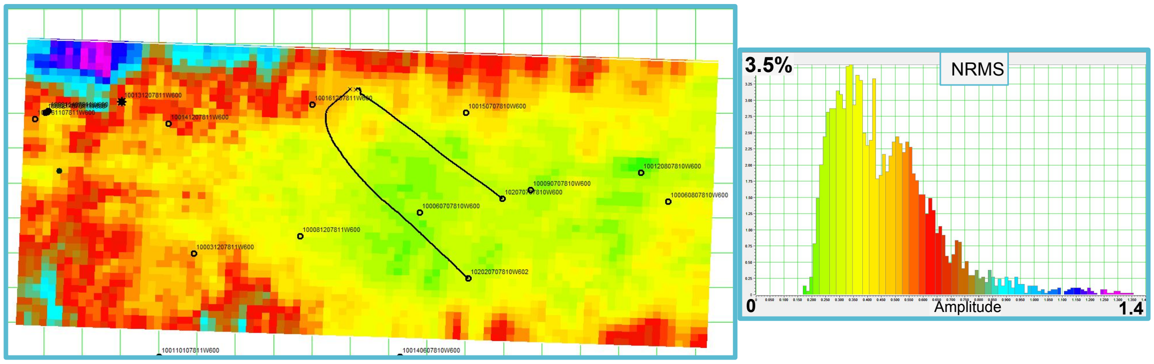

Figure 2.9: NRMS map and histogram for Monitor 2 minus Baseline (most recent processing results).

2.5 Overburden Layer Stripping

Layer stripping was conducted on all three vintages of the Pouce Coupe time-lapse, converted-wave seismic data. This section describes the pre-stack methodology of determining the anisotropy (shear-wave splitting analysis) and layer-stripping procedure, and the final volumes output for interpretation by Sensor Geophysical.

Reflected converted waves recorded at the receiver are encoded with the propagation effects of the overburden layers as they travel from the reservoir zone back to the surface; therefore, to accurately characterize the anisotropy within the reservoir interval, the overburden shear-wave splitting effect must be removed as discussed by Grossman and Steinhoff (2013). Layer stripping in this context refers to replacing any anisotropic layers with effectively isotropic layers. Removal of any shear-wave splitting effects from all layers above the reservoir has become a rigorous process to increase the quality of interpretation of anisotropic effects at the reservoir level.

Shear-wave splitting analysis is not new but significant improvements have recently been made in the algorithms for determining the magnitude and orientations of the split waves. Typically, most methods relied on removing the splitting effects by minimizing the energy on the transverse component. This methodology works well in estimating the fast converted-wave polarization and time delays in areas of high anisotropy because in this case the energy on the transverse component is significantly above the noise level. When the shear-wave splitting is weak, typical of deeper anisotropic layers, the analysis is more rigorously performed by maximizing the stack power of the radial component (Li and Grossman, 2012).

Limited azimuth stacks (LAS) are created by forming supergathers of all azimuths ($0 - 360^0$) at a certain asymptotic conversion point (ACP), then sectoring stacks into 10^0 azimuth bins for analysis (Figure 2.10). These stacks are diagnostic of shear-wave splitting which is clearly present here on both the radial and transverse components. The radial component shows azimuthal variation in arrival times at various reflection events (yellow curve), the early (fast) arrivals of the sinusoidal events correspond to the fast shear-wave (S_1- or PS_1-wave)

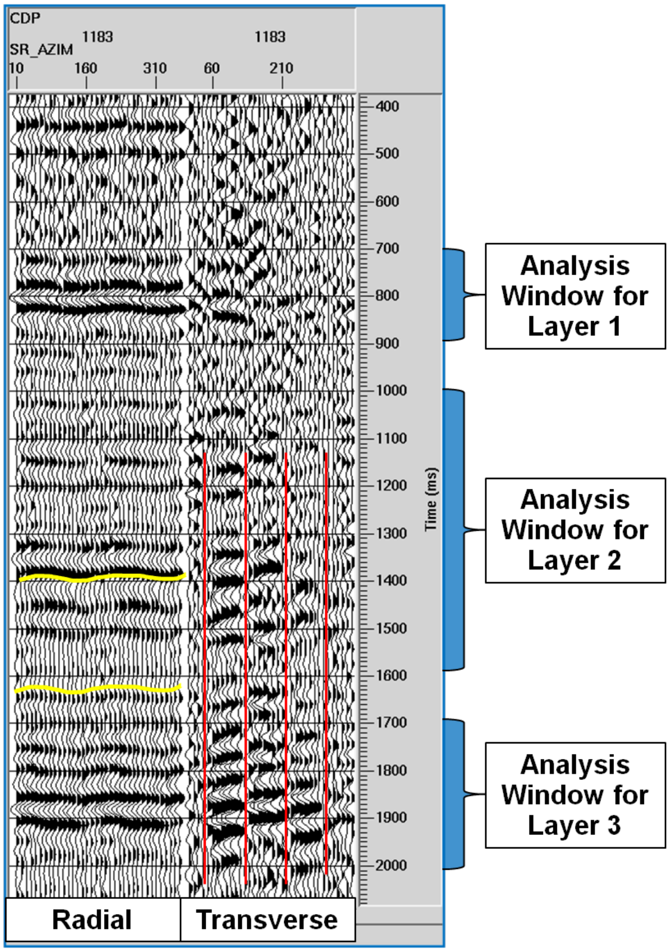

Figure 2.10: Limited azimuth stack (LAS) at ACP 1183. The anisotropic character is shown by the sinusoidal variations on the radial component and the switch in polarity on the transverse component. The early arrival time of the radial sinusoid corresponds to the fast PS-wave (PS_1-wave) arrival azimuth and the point of the polarity change on the transverse component indicates the crossing of the S_1-wave or S_2-wave axis.

polarization, while the late (slow) arrivals occurring at 90^0 away, correspond to the slow shear-wave (S_2- or PS_2-wave) polarization. On the traverse component, the polarity change indicates whenever the S_1 or S_2 axis has been crossed (vertical red lines in Figure 2.10). Using these two azimuthal characteristics, the polarization orientations of the fast and slow shear waves were uniquely determined.

The layer stripping process involves scanning over the full range of trial fast converted-wave (PS_1-wave) polarization azimuths. For each azimuth, the data were rotated into a trial PS_1- and PS_2-wave coordinate system, then a suite of trial time delays are used to “layer strip" the data, and the corresponding suite of results are analyzed upon transformation back to R, T coordinates. The process than involves optimization of an objective function to find the best fit solution; most of the methods currently in use rely on the objective of minimizing the distribution of energy remaining on the transverse component after layer stripping. In comparison, the methodology of layer stripping utilized for processing the Pouce Coupe seismic data was a radial-component-based objective to maximize the coherence of the shear-wave energy transferred onto the radial component (Li and Grossman, 2012).

Pre-stack layer stripping is done in the following steps: for each azimuth the data was rotate the coordinates from R, T (radial/transverse) to the trial PS_1- and PS_2-wave polarization orientations, then all trial time shifts are used to align (in time) the PS_2 event with the matching PS_1 event and then corresponding results are stacked and the radial stacking power is analyzed. By repeating over all trial polarization azimuths for the PS_1-wave, the optimal solution corresponds to the maximizing of coherence of the shear-wave energy transferred onto the radial component. After the time delays are established for the splitting analysis window they are removed and the data is reset into the R', T' (radial/transverse prime) coordinate system. This process was repeated down the section over multiple windows, in our case three (700-900ms, 1000-1600ms, 1700-2000ms), until the top of the Montney reservoir was reached at 2100ms.

The time delays and PS_1-wave polarization azimuths resulting from the layer stripped window are displayed for the Baseline Pouce Coupe time-lapse seismic survey in Figure 2.11. The color scale represents the magnitude of time delays between PS_1 and PS_2 events and the needle represents the orientation of the estimated PS_1-wave polarization. As expected, the near surface (Layer 1) has the highest anisotropy with time delays up to 6ms (Layer 1 in Figure 2.11). Layers 2 and 3 have significantly lower time-delay magnitudes, and the $P_2 - P_1$ time delays and PS_1-wave polarizations for these two layers do not vary significantly. The smooth and vertically stable behavior give confidence in the layer stripping result.

In the reservoir interval, the pre-stack shear-wave splitting analysis rotated the data into the correct PS_1- and PS_2-wave polarizations, while leaving the time delays intact for post-stack shear-wave splitting analysis. Although the time delays are not “stripped”, the shear-wave splitting analysis (time delays and PS_1-wave polarization azimuths estimates) for the reservoir level are displayed for all three vintages of the Pouce Coupe time-lapse seismic survey in Figure 2.12. The final window used for the splitting analysis was taken at 2150-2450 ms, which was beneath the reservoir interval (2100-2300 ms) and chosen in this way to account for the reflections that travel upward through the reservoir interval. At the reservoir the maximum estimated time-delay was only about 4 ms, and correlates with the expected reservoir activity and regions of increasing time delay over the duration of the survey. The PS_1-wave polarization remain quite laterally stable over each survey and also consistent between the three acquisitions vintages.

2.6 Processing Conclusion

The processing flow performed by Sensor Geophysical encompasses many substantial enhancements in the processing of converted-wave data for time-lapse shear-wave splitting analysis. The main steps outlined are believed to contribute most to the high quality final processing product, including: RADAR, simultaneous processing, shear-wave splitting analysis and layer stripping. RADAR was uses as a correction of vector infidelity problems caused by misaligned receivers in the field and was found to greatly increase the signal-to-noise ratio and reduce leakage into the transverse components. The time-lapse data were processed using NRMS-guided simultaneous processing; the goal was to maximize the repeatability between surveys allowing time-lapse changes within the reservoir to be confidently interpreted. After performing the simultaneous processing the data were sufficiently repeatable for time-lapse interpretation and further cross-equalization done post-stack was not required. Improved shear-wave splitting analysis for layer stripping the overburden anisotropy effects and proper rotation into PS_1- and PS_2-wave polarization azimuths within the reservoir interval was crucial. Using the radial component maximum stack power method resulted in great improvements in determining the orientation and magnitude of shear-wave splitting, and more critically was very stable when rotating the data into the PS_1- and PS_2-wave volumes for reservoir characterization.

The final output of the processing sequence are layer-stripped radial and transverse stacks that are orientated to the proper PS_1- and PS_2-wave polarizations at the reservoir interval. Above the reservoir interval the data represents a time delay stripped radial and transverse volume (R' volume and a T' volume, respectively) (Figure 2.13). The output stacks are deemed adequate for detailed post-stack shear-wave splitting analysis.

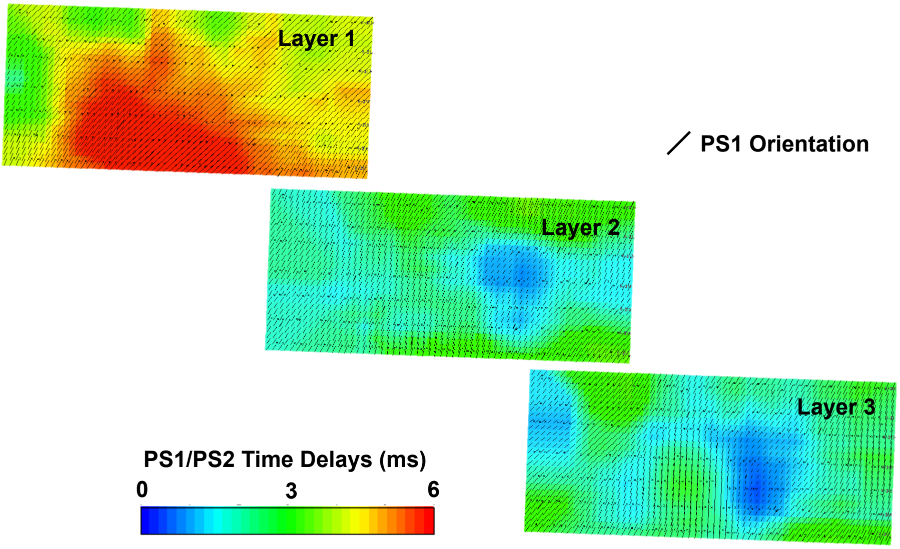

Figure 2.11: Overburden splitting for each analysis window, representing the anisotropy stripped at each layer. Layers 1 (700-900ms), Layer 2 (1000-1600ms) and Layer 3 (1700-2000ms). The color scale represents the magnitude of time delays between PS_1 and PS_2 events and the needle represents the orientation of the estimated PS_1-wave polarization.

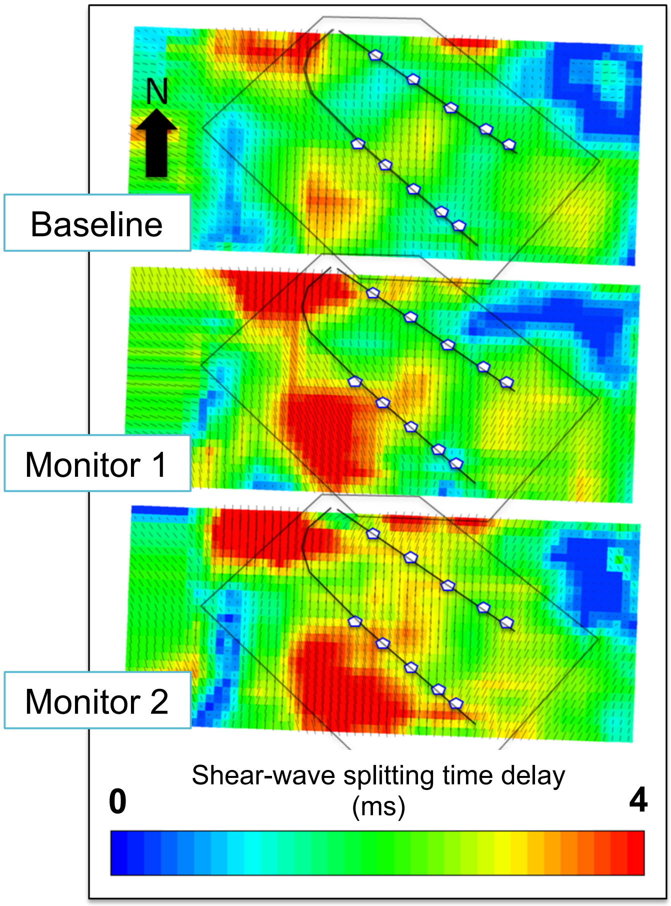

Figure 2.12: Prestack time delay and PS_1-wave polarization estimates at the reservoir level, displayed for all three vintages of the Pouce Coupe time-lapse seismic survey. The color scale represents the estimated time delays between PS_1 and PS_2 events while the needle length and orientation represent the estimated PS_1-wave polarizations. The black polygon drawn on each map bounds the area of interest for this study, and the wells are displayed along with hydraulic fracture stages locations indicated by the small pentagons (Grossman and Steinhoff, 2013).

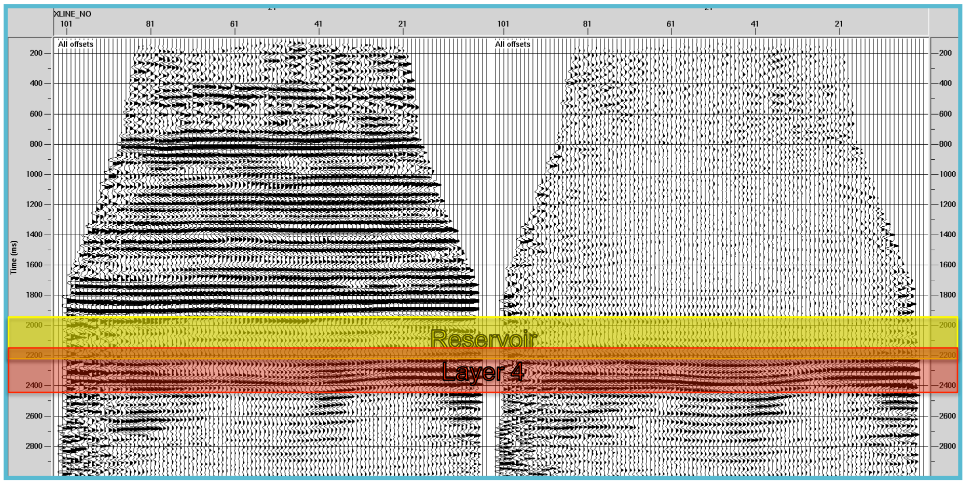

Figure 2.13: Final stack (all offsets) result of converted-wave data after processing and layer stripping. PS_1- and PS_2-wave are orientated for the reservoir interval and above the reservoir the data represents R' and T'. The reservoir interval is located between 2100-2350ms (outlined in yellow). The final window for the shear-wave splitting analysis is shown by layer 4 (2150-2450ms).

CHAPTER 3

TIME-LAPSE, MULTICOMPONENT SEISMIC

3.1 Introduction

The Pouce Coupe time-lapse, multicomponent surface seismic data were acquired in 2008 by Talisman Energy Inc. to characterize and monitor changes caused by hydraulic stimulation within the shale reservoir. Geophones were permanently installed and the shot holes cased for optimum repeatability characteristics. The architecture of the acquisition was designed for full 360-degree coverage and offset distribution interpolated to a bin size of 50 m by 50 m. The data set includes a baseline survey acquired after drilling the two horizontal NW-SE trending wells (wells 2-07 and 7-07) (Figure 3.1). Monitor 1 was acquired after the hydraulic fracture stimulation of the 2-07 well and only slight flow back to keep high reservoir pressurization. Following the hydraulic stimulation of the 7-07 well, Monitor 2 was acquired to characterize the overall stimulation over the two horizontal wells (Figure 1.7).

The fracture treatment was expected to induce anisotropy, or increase shear-wave splitting, most in the areas where the natural fracture density was highest, due to the ease of energy propagation in highly fractured reservoir rock. By comparing shear-wave splitting before and after the fracture treatment, the effective stimulated volume should be identifiable.

In comparison to converted-wave surface seismic monitoring, microseismic surveys monitor the volume of reservoir that has reacted to the hydraulic fracture treatment (stimulated reservoir volume) but little can be deduced from this data about how fractures react after proppant is distributed to keep the fracture permeability pathways open (referred to as the effective stimulated volume). To ultimately correlate production to the hydraulic stimulation success the effective stimulated volume associated with high permeability pathways must be determined. Hydraulic stimulation monitoring is one application of multicomponent technology where the use of converted-waves for imaging reservoir anisotropy exhibits great

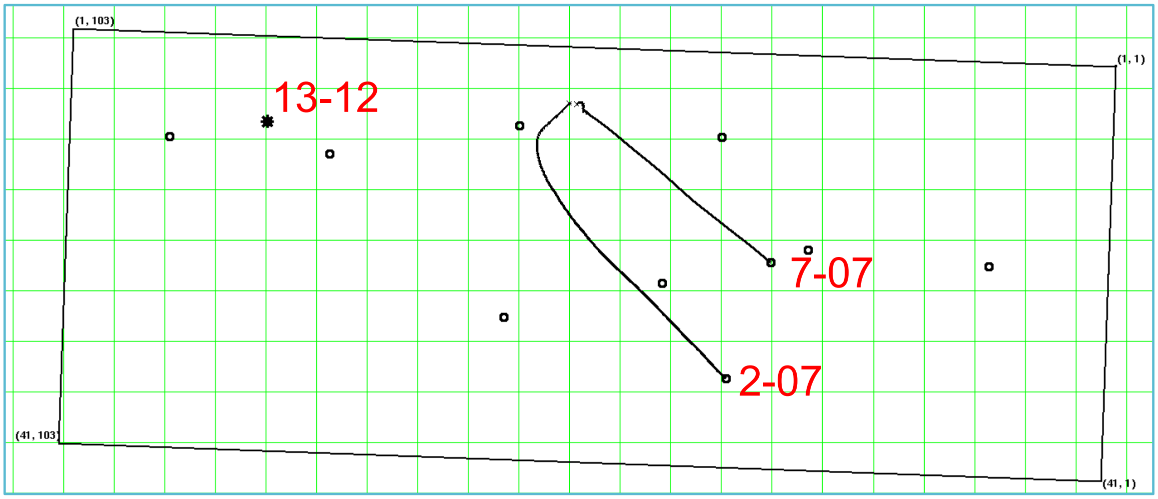

Figure 3.1: Seismic survey boundary in black (inline 1-41, crossline 1-103). Two horizontal wells (2-07 and 7-07) and the vertical 13-12 well containing the vertical shear sonic log.

benefit.

3.2 Well Tie

Figure 3.2 shows the well tie of the fast converted-wave volume (PS_1-wave) at the 13-12 vertical well (Figure 3.1) using a statistically extracted wavelet and the acquired shear sonic log. A good tie was achieved from the top of the Gething down into the Montney interval without any phase rotation. At this location, the top of the Montney is a relatively weak peak and becomes more definitive as you move laterally to the East. The top of the Montney was picked on the seismic as the Montney E marker. The 13-12 well does not penetrate the entire Montney section, though it is known that the peak event at 2300 ms (PS-time) corresponds to the Montney-Belloy unconformity and exhibits consistent reflectivity across the entire survey area.

3.3 Field Scale Seismic Interpretation

To examine the influence of the Montney structure and link it to the hydraulic stimulation control, both isochrons and fault mapping were utilized. From the seismic cross-section

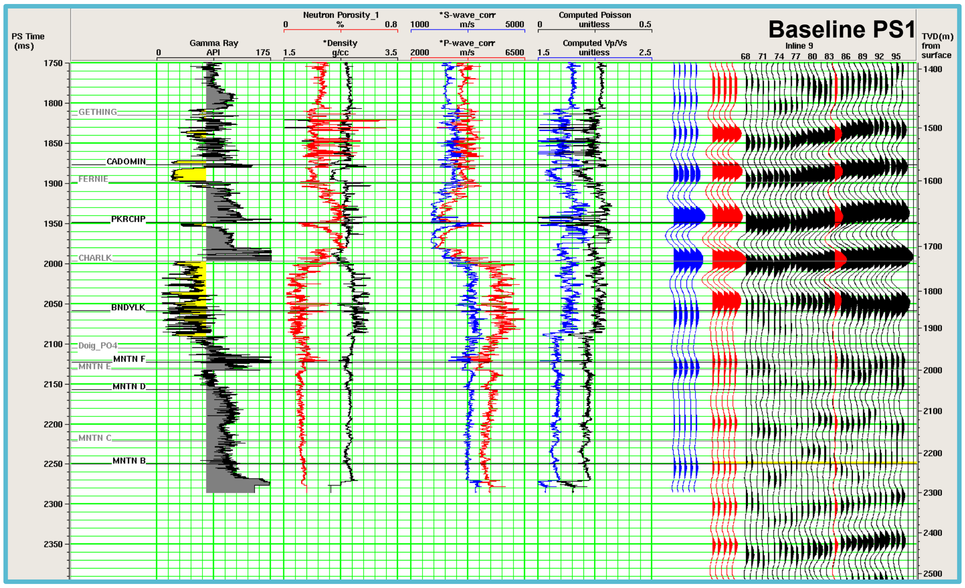

Figure 3.2: 13-12 vertical well tie with Baseline fast converted-wave (PS_1-wave) seismic.

and the Montney isochron calculated between the Belloy and Montney E marker (BLLY-MNTN E), a localized isochron thick (in PS-time) is apparent in the middle of the survey (Figure 3.3).

The influence of the observable low of the seismic mapping exhibits to have structurally controlled the deposition of the Montney package, but the impact becomes less significant for the Upper Montney units (Figure 3.3), as stated in Section 1.1.1. The mapped low controls the local thickness variations in the Lower Montney. Thickness variations are believed to be governed by the Paleozoic surface highs and lows generated with the re-activation of basement faults (see Sections 1.1, 1.1.1 and 1.1.2).

In the Pouce Coupe Field, multicomponent seismic discontinuities present in the PS_1- and PS_2-wave seismic images do not exhibit an observable reflector displacement; they have been interpreted as minimal offset faults corresponding to strike-slip/wrench faults, typical of the faulting system in the Peace River Arch (Figure 3.4). The faulting within the Montney reservoir unit was interpreted using the offset of deeper reflectors as guides and continued upward to where dimming occurred in the Montney interval. Two main fault trends are present in the data, NE-SW and NW-SE; these are believed to be related to the thickness

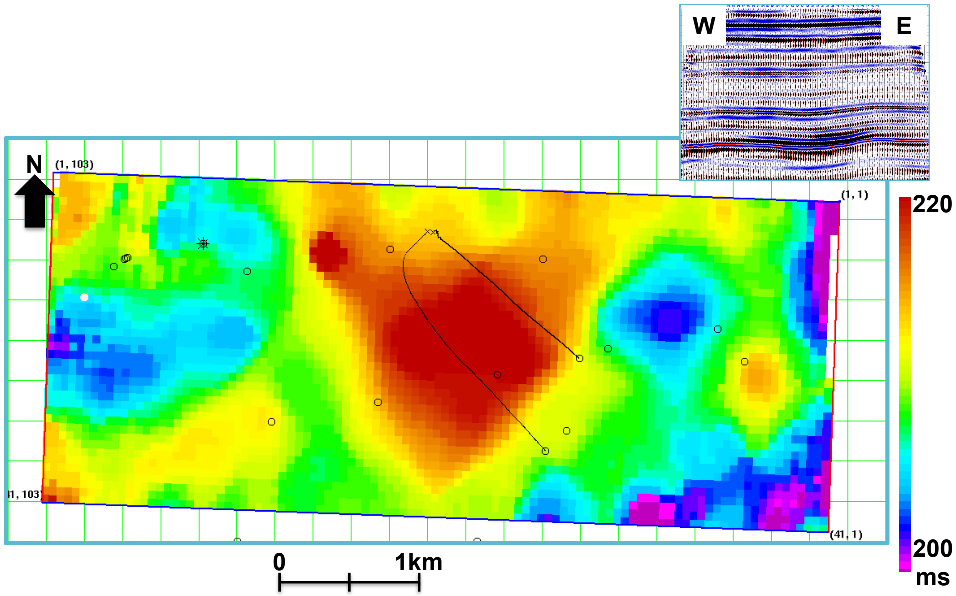

Figure 3.3: Montney isochron (BLLY-MNTN E) generated from the PS_1-wave seismic data. Horizontal wells 2-07 and 7-07 intersect the thickest (in time) part of the Montney reservoir.

variations of the Montney (Figure 3.4).

The dimming associated with the interpreted fault lineaments may be characteristic of fault damage zones, or locations of higher fracture density. These fault lineaments could also be areas of increased or perturbed stress, and increased likelihood of fracture failure if in close proximity to the hydraulic stimulation. Depending on the fracture orientation relative to the hydraulic fracture treatment, they could inhibit the lateral growth of the induced fracture network.

3.4 Fracture Characterization Methodology

In this section, the key concepts of imaging natural and induced fracture networks with converted-wave surface seismic data are introduced. First, I discuss the theory behind shear-wave splitting and how is it used to characterize dominant fracture orientation and density. Also described are interpretation procedures and how the shear-wave splitting anomalies relate to fracture-enhanced hydrocarbon flow.

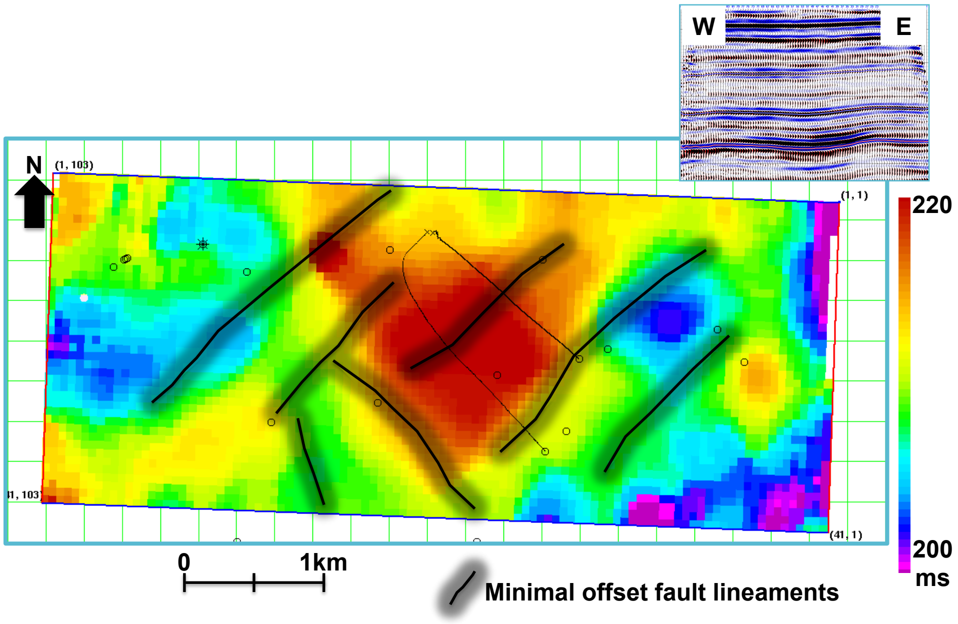

Figure 3.4: Interpreted minimal offset fault lineaments from PS_1- and PS_2-wave seismic volumes overlain on MNTN isochron (BLLY-MNTN E (Figure 3.3)) Bed offset of deeper horizons were interpolated into the Montney and above formations and picked where dimming tracked the same fault trends. Two main trends are present in the data, NE-SW and NW-SE, characteristic of wrench faulting systems in the Peace River Arch.

3.4.1 Shear-wave Splitting Theory

Open fractures within the reservoir rock may create permeability pathways and cause the shear-wave velocities to be different parallel and perpendicular to the open fracture planes. If an incident shear-wave is polarized in a direction neither parallel nor perpendicular to the fractures, it will split into a fast and slow mode, which is commonly referred to as shear-wave splitting. Analysis of the split shear-waves provides the ability to determine the shear-wave splitting coefficient ($\gamma^{(s)}$) and the shear-wave polarizations determined by the fracture orientations.

The shear-wave splitting coefficient ($\gamma^{(s)}$) is a combination of Thomsen-style parameters for general orthorhombic media (Tsvankin, 2012b):

$$\gamma^{(s)} \approx \gamma^{(1)} - \gamma^{(2)} \tag{3.1}$$

For the specific model of a vertically traveling shear-wave through two rotationally invariant vertical orthogonal fracture sets in a purely isotropic host rock (Figure 3.5). The anisotropy coefficient $\gamma^{(2)}$ is defined in the $[x_1, x_3]$- plane and depends on the density (e_1) of the fracture set orthogonal to the x_1-axis. Similarly, $\gamma^{(1)}$ is governed by the density (e_2) of the second fracture set.

Shear-wave splitting at near vertical-incidence is described by the fractional difference between the stiffness coefficients c_{44} and c_{55} or, approximately, the fast and slow shear-wave velocities:

$$\gamma^{(s)} \equiv \frac{c_{44} - c_{55}}{2c_{55}} \approx \frac{V_{S1} - V_{S2}}{V_{S2}} \tag{3.2}$$

where $V_{S1} \equiv \sqrt{\frac{c_{44}}{\rho}}$ is the vertical velocity of the fast shear-wave (S_1) and $V_{S2} \equiv \sqrt{\frac{c_{55}}{\rho}}$ is the vertical velocity of the slow shear-wave (S_2).

The fast shear-wave polarization corresponds to the dominant open fracture orientation (Figure 3.5) and the magnitude of shear-wave splitting is proportional to the difference

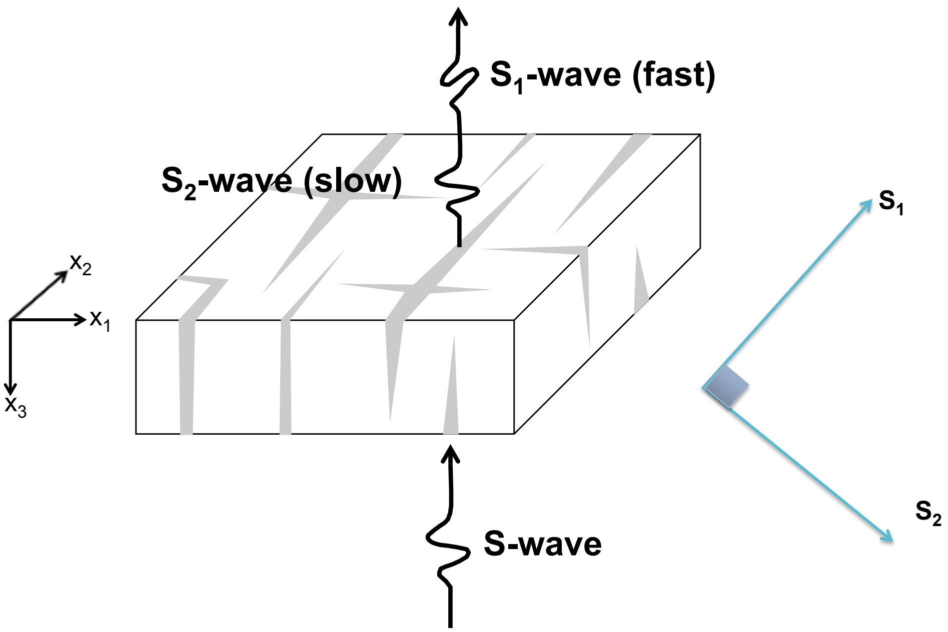

Figure 3.5: Shear-wave splitting in orthorhombic media, formed by two orthogonal sets of vertical fractures. A vertically traveling S-wave will split into two waves traveling at different velocities. The fast shear-wave (S_1) is polarized parallel to dominant fracture orientation while the slow shear-wave (S_2) is polarized in the x_1 direction (after Terrell (2004)).

between the crack densities of two dominant fracture sets ($e_1 - e_2$) (Tsvankin and Grechka, 2011):

$$\gamma^{(s)} = \frac{8}{3}(e_1 - e_2)\frac{\lambda_b + 2\mu_b}{3\lambda_b + 4\mu_b} \tag{3.3}$$

λ_b and μ_b are the Lame constants of the isotropic background assumed over the reservoir interval and the fraction containing both constants to approximately equal unity (Bakulin et al., 2000). The shear-wave splitting coefficient is approximately equal to:

$$\gamma^{(s)} \approx e_1 - e_2 \tag{3.4}$$

Further generalization to multiple fracture systems of arbitrary orientation embedded in an isotropic background rock approximately leads to effective orthorhombic symmetry (Vasconcelous and Grechka, 2007). For long seismic wavelengths, multiple arbitrarily oriented vertical fractures are approximately equivalent to two mutually orthogonal fracture sets referred to as the principal fracture sets. Utilizing the effective orthorhombic fracture model we can measure shear-wave splitting of multiple fracture sets.

Shear-wave splitting can characterize a single vertical fracture set embedded in an isotropic matrix. This type of model is referred to as horizontal transverse isotropy (HTI) (Figure 3.6) and is described by Tsvankin (2012b) and Tsvankin (1997b). The HTI model has a symmetry axis perpendicular to the fracture planes and an isotropy plane parallel to the fracture. For this case, the coefficient ($\gamma^{(1)}$) goes to zero if the symmetry axis is parallel to x_1. In HTI media, which can be treated as a degenerate case of orthorhombic symmetry, the splitting coefficient becomes:

$$\gamma^{(s)} \approx \gamma^{(2)} = \frac{V_{S1} - V_{S2}}{V_{S2}} \tag{3.5}$$

The shear-wave splitting coefficient ($\gamma^{(s)}$) has the same form for a general orthorhombic model or HTI model. The coefficient ($\gamma^{(s)}$) can be calculated from the vertical S-wave velocities or, equivalently, time delay between split shear-waves at vertical incidence:

$$\gamma^{(s)} \approx \frac{t_{S2} - t_{S1}}{t_{S1}} \tag{3.6}$$

The shear-wave splitting coefficient may be obtained from the surface measured interval travel-times of the fast and slow shear-waves corresponding to the same subsurface layer. Multiplying the splitting coefficient by 100 gives the percentage difference between the vertical velocities of the split shear-waves.

3.4.2 Shear-wave Splitting Interpretation Methodology

This section describes how the shear-wave splitting theory described in the previous section is used to interpret the reservoir anisotropy for fracture characterization. The orientation and magnitude of shear-wave splitting are related to discontinuities within the

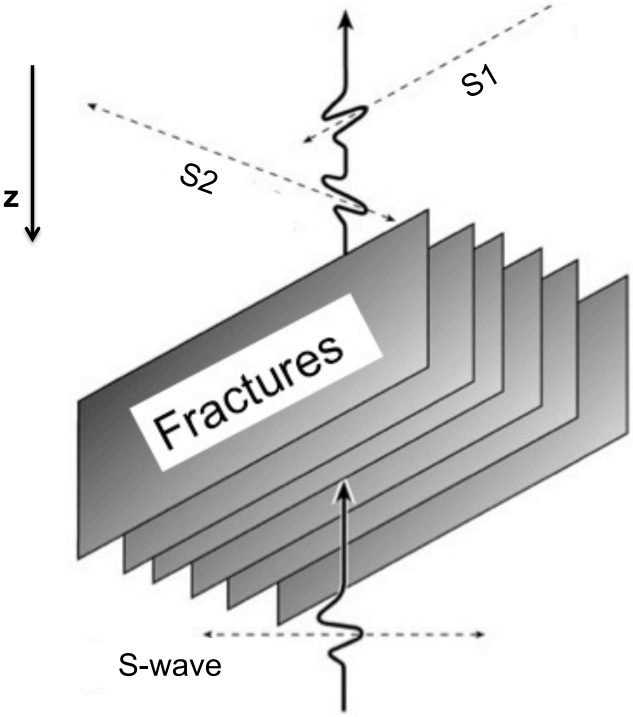

Figure 3.6: Shear-wave splitting in HTI, formed by parallel vertically fractures. A vertically traveling S-wave will split into two waves traveling at different velocities, polarized parallel to fractures (fast - S_1) and orthogonal (slow - S_2). Modified from Hardage et al. (2011).

background rock caused by open fractures. Monitored changes in the shear-wave splitting magnitude caused by hydraulic stimulations are related to the effective fracture permeability (connected fractures) and preferential hydrocarbon flow directions. In comparison, microseismic surveys attempt to monitor the volume of reservoir that has reacted to the hydraulic fracture treatment (stimulated reservoir volume) but it is unknown how fractures react after proppant is distributed to keep the fracture pathways open.

The PS_1- and PS_2-wave stack seismic volumes (final stacks displayed in Figure 2.13) allow for the vertical shear-wave splitting time delays to be analyzed. In this analysis, the post-stack approach of estimating shear-wave splitting is an interval time based measurement of the converted-waves (S_1 and S_2 equivalent to PS_1 and PS_2, respectively)(Equation 3.7). Due to the lack of coherent reflectors within the reservoir, shear-wave splitting was calculated from the seismic marker at the base of the reservoir (Figure 3.7). This method estimates an effective shear-wave splitting over the entire reservoir interval and assumes the dominant fracture orientation does not vary vertically. From microseismic observations, it is concluded that hydraulic fractures are both laterally and vertical contained within the reservoir interval; therefore, effective shear-wave splitting magnitude is believed to sufficiently quantify the induced fracture network.

$$\gamma^{(s)} \approx \frac{t_{PS2} - t_{PS1}}{t_{PS1}} \tag{3.7}$$

Image log analysis determined that within the reservoir, two almost vertical fracture sets exist roughly orthogonal to each other. Typically at each well location 65% of fractures imaged are in the dominant orientation while about 5% are in the perpendicular orientation. As a result, the fracture characteristics of the Montney should cause observable shear-wave splitting and allow for an accurate measurement the dominant fracture orientation and fracture density differences.

Time-lapse shear-wave splitting interpretation has been limited to the polygon in Figure 2.8 corresponding to the reliable shear-wave splitting analysis window (layer stripping and determination of PS_1-wave polarization within the reservoir) and high repeatability for time-lapse changes. Areas outside this polygon are deemed unreliable due to poor data quality from low fold. Other shear-wave splitting analysis limitations are due to the recording and survey bin size. The data were recorded at a 2ms sample rate; resulting in an expected resolvable change of the shear-wave splitting ($\gamma^{(s)}$) lower than 0.8%, due to the interpolated waveform picking. Also, lateral variations of shear-wave splitting are limited to the 50m by 50m bin size and interpreted as effective anisotropy of each bin area.

Interpretation of shear-wave splitting is based on the orthogonal fracture set model (Figure 3.5). PS_1-wave polarizations is indicative of the more dominant fracture orientation and the magnitude of shear-wave splitting is interpreted to be related to the difference in fracture densities.

Increased shear-wave splitting after hydraulic fracturing is assumed to correspond to connected fractures, propped fracture volume or the effective stimulated volume. This interpretation relies on the assumption that inducing fractures at a distance from the well is caused by hydraulic fracturing fluid traveling through connected fracture permeability to reach the extent of the shear-wave splitting anomaly. On the other hand, Baseline shear-wave splitting due to natural fractures does not have to correspond to the effective permeability, because not all fracture networks have to be connected.

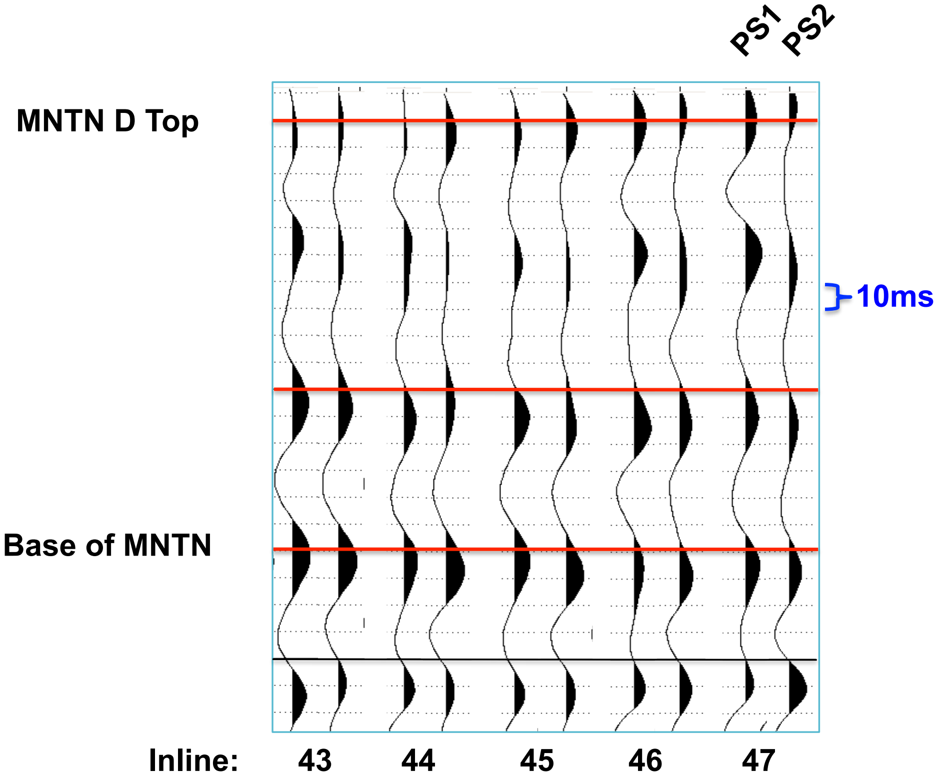

Figure 3.7: Shear-wave splitting time delays, calculated by taking the base of the reservoir horizon time difference between PS_1- and PS_2-wave for each inline location.

CHAPTER 4

SHEAR-WAVE SPLITTING INTERPRETATION

4.1 Introduction

In this section, the shear-wave splitting occurring within the reservoir interval is discussed for each time-lapse seismic survey representing a specific . Then time-lapse differences in shear-wave splitting are interpreted for hydraulic fracture monitoring and the determination of the effective stimulated volume. The shear-wave splitting results are then correlated to the microseismic interpretations and production data.

4.2 Baseline Shear-wave Splitting Results

The Baseline survey shear-wave splitting are used to characterize the in-situ fracture conditions. Determining the natural fracture properties before hydraulic stimulations is crucial from the geomechanical perspective. The hypothesis is that natural fractures control the propagation of hydraulic stimulation energy.

Based on the PS_1-wave polarization orientation determined by the pre-stack shear-wave splitting analysis in Layer 4 (Figure 4.1), it was observed that the principal fast shear-wave orientation varies over the local field scale and may correspond to variations in the dominance of the main fracture orientation (see section 1.5.5). The dominant fracture orientation near horizontal 7-07 well corresponds to the S_{Hmax} orientation (N40^0E) while in the vicinity of the horizontal 2-07 well, the PS_1-wave polarization takes the orthogonal direction, with an exception near Stage 1 at the well toe (Figure 4.1).

The Baseline shear-wave splitting show natural shear-wave splitting conditions – less than 3 % (Figure 4.1). The low Baseline shear-wave splitting values may be due to a lack of in-situ fractures or the two orthogonal fracture sets are roughly equal in intensity. Although the anomalies are restricted to small spatial areas, the shear-wave splitting map exhibits two main trends orientated northwest and northeast, intersecting the horizontal wells.

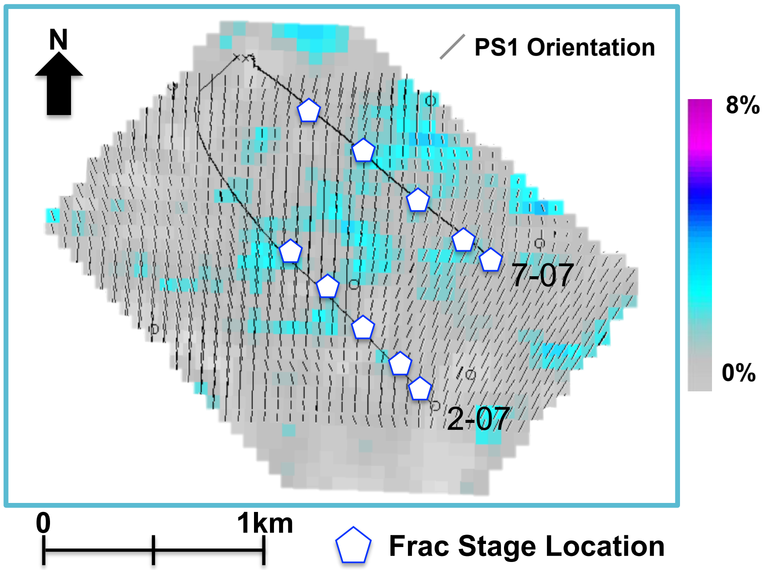

Figure 4.1: Baseline shear-wave splitting magnitude (color) and PS_1-wave polarization orientation (needle).

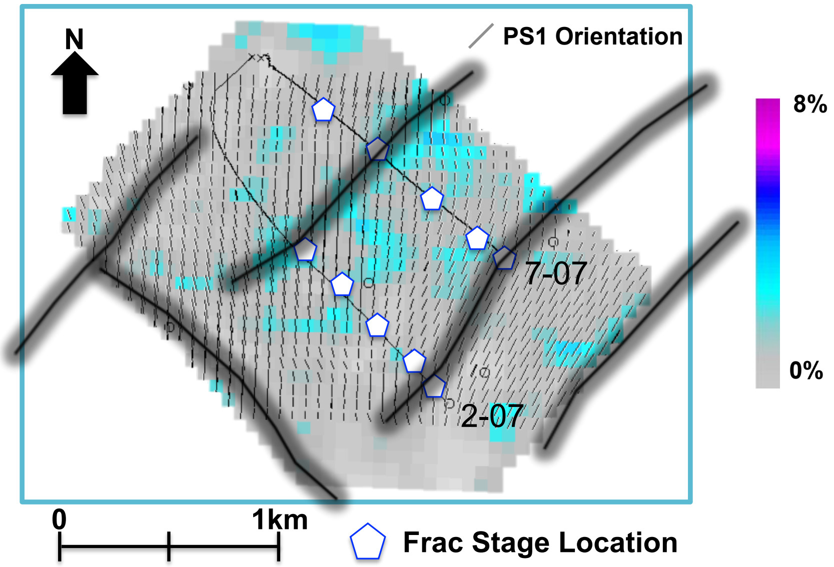

Figure 4.2: Baseline shear-wave splitting magnitude and PS_1-wave polarization orientation. Independent fault interpretations from PS_1- and PS_2-wave seismic volumes overlain.

4.3 Monitoring 1 Shear-wave Splitting Results

The Monitor 1 survey is used to determine the induced hydraulic fracturing effect for the horizontal 2-07 well because it was acquired after the stimulation of the 2-07 well but before the stimulation of the 7-07 well. After the stimulation, three prominent induced shear-wave splitting anomalies are present (Figure 4.3). The linear anomaly (NE-SW) at the southern Stage 1 (toe) portion have magnitude 3 to 5% shear-wave splitting and may be associated with the minimum offset fault lineament that are interpreted in Figure 3.4. The induced shear-wave splitting anomaly extends in a classic symmetric bi-wing pattern parallel to the present-day regional maximum horizontal stress direction ($N40^0E$), with an interpreted fracture half-length estimated to be 250 m.

The shear-wave splitting anomaly located are stages 3 and 4 varies in magnitude between 3 to 8% and builds mainly south of the wellbore. The trend of hydraulic energy propagation could be due to the dominant fracture orientation changing along the horizontal 2-07 well, perhaps representing a stress concentration and preferential fracturing conditions. This anomalies growth may be indicative of the hydraulic fracture propagation in the regional S_{Hmax} direction and the tensile opening of a dominant fracture set.

The shear-wave splitting anomaly near the heel of the well (Stage 5) increases in magnitude and exhibits the same shape as present in the Baseline shear-wave splitting (Figure 4.1). The anomaly has a symmetric pattern in both of the dominant natural fracture orientation (northeast) and against the predominant fracture fabric (southwest). Due to the interpreted orthogonal fracture sets, this type of behavior is not unexpected.

4.4 Monitoring 2 Shear-wave Splitting Results

Figure 4.5 shows the overall hydraulic stimulation effect for both of the two horizontal wells because it was acquired after stimulation of both the 2-07 and 7-07 wells. The 7-07 well stimulation does not seem to create a strong shear-wave splitting response. The NE-SW anomaly created during the 2-07 well stimulation continues to grow in magnitude

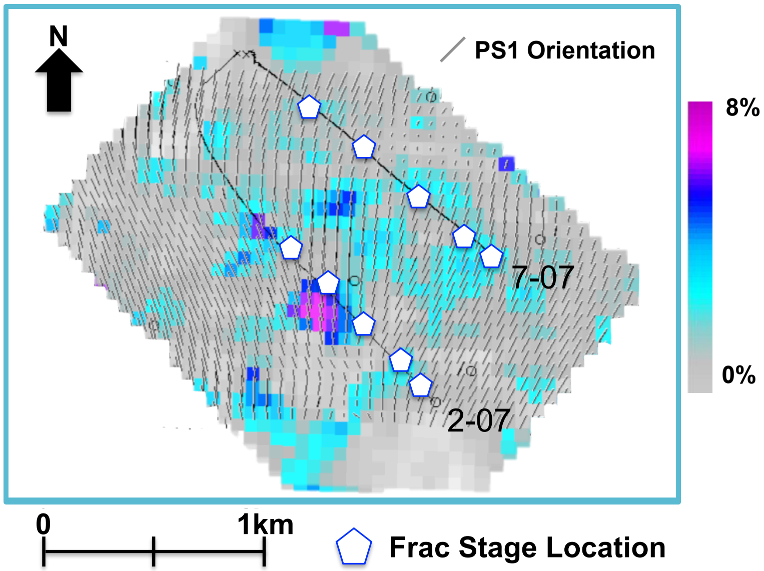

Figure 4.3: Monitor 1 shear-wave splitting magnitude (color) and PS_1-wave polarization orientation (needle).

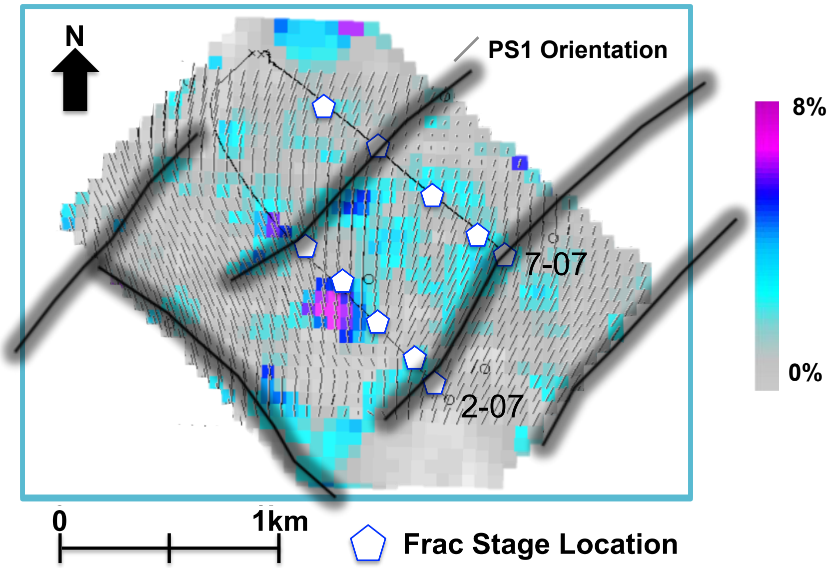

Figure 4.4: Monitor 1 shear-wave splitting magnitude (color) and PS_1-wave polarization orientation (needle). Independent fault interpretations from PS_1- and PS_2-wave seismic volumes overlain.

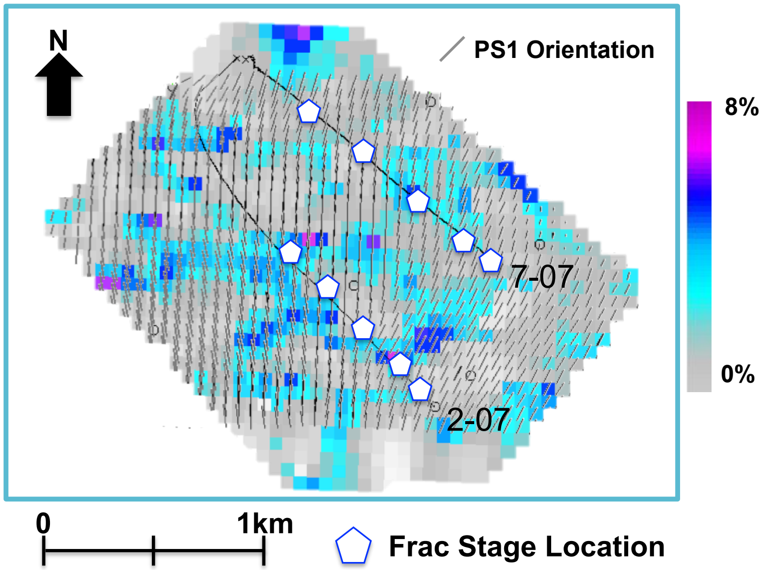

Figure 4.5: Monitor 2 shear-wave splitting magnitude (color) and PS_1-wave polarization orientation (needle).

(Figure 4.7). It was observed in the microseismic mapping result that the majority of the hydraulic stimulation energy was focused into what is interpreted as open fractures related to the previously interpreted minimal offset fault lineament at the toe of the well (Figure 4.5).

The two anomalies near the 2-07 well previously discussed (Figure 4.1 and Figure 4.3) have by this time decreased in magnitude and have become much more spatially diffuse. The decrease in magnitude and increase in spatial area could represent the equilibrating of stimulation pressure. The decrease in magnitude could also suggest that the fractures are closing on the proppant and therefore, decreasing the shear-wave splitting magnitude.

The time-lapse response caused by the hydraulic stimulations were predominantly manifested as changes in the shear-wave splitting. Dominant fracture orientations (or PS_1-wave polarization) did not change significantly between the Baseline and monitoring surveys, implying that the hydraulic stimulation energy is mainly affecting the natural fractures and that the induced shear-wave splitting anomalies may correspond, at least temporarily, to propping of the pre-existing fracture network.

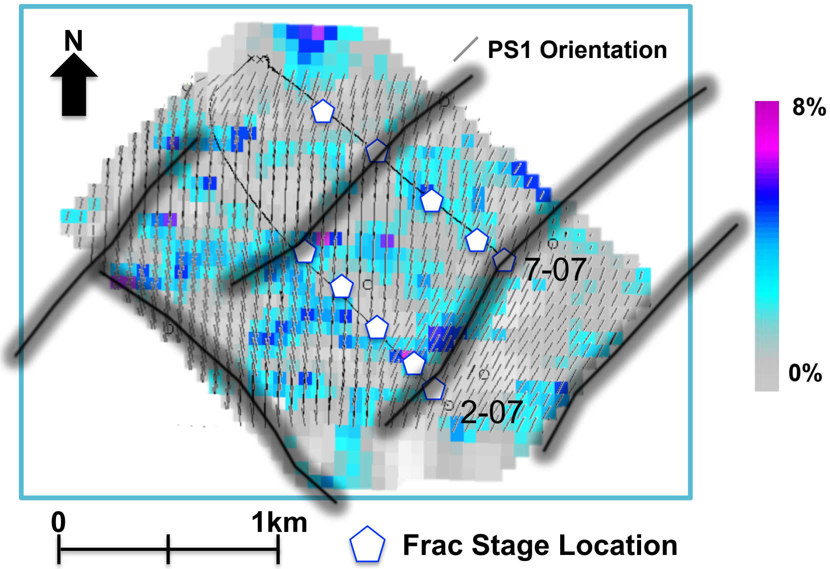

Figure 4.6: Monitor 2 shear-wave splitting magnitude (color) and PS_1-wave polarization orientation (needle). Overlain are independent fault interpretations from PS_1- and PS_2-wave seismic volumes.

4.5 Shear-wave Splitting Time-lapse Differences

Shear-wave splitting time-lapse differences provide insight into the pre-existing and induced anisotropy. Monitoring the shear-wave splitting is somewhat equivalent to microseismic monitoring in principle.

It was concluded in the previous discussions of the shear-wave splitting results, that dominant fracture orientation does not vary significantly between seismic surveys. The more important changes in shear-wave splitting magnitude are summarized in (Figure 4.7). Increased shear-wave splitting in previous anomalies suggest the stimulation of the dominant natural fracture orientation.

Shear-wave splitting anomalies, or the lack there-of, become more apparent by differencing the calculated shear-wave splitting (Figure 4.7). From these difference maps, the overall stimulation of each well can be determined. The results relate to the stimulation of natural fractures that may have not been previously opened and now may provide effective conduits to the wellbores.

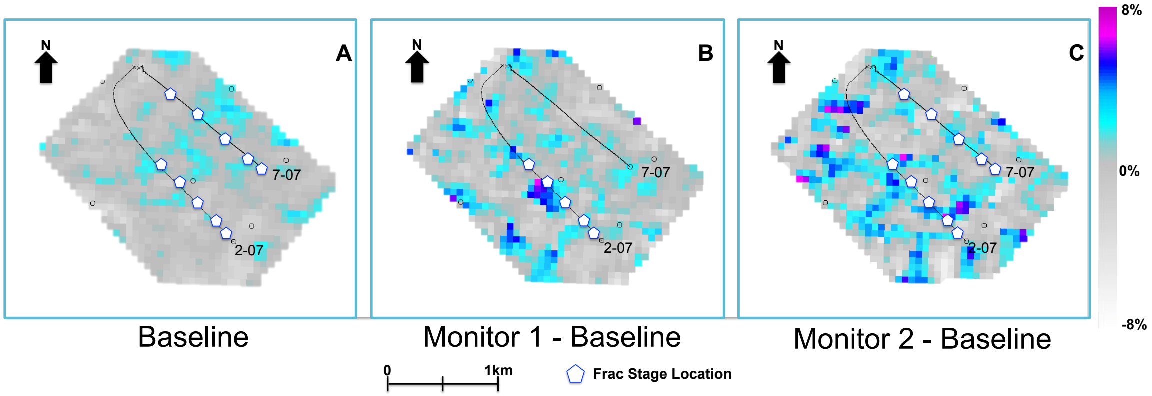
Baseline

Monitor 1 - Baseline

Monitor 2 - Baseline

Figure 4.7: Shear-wave splitting - (A) Baseline, (B) Monitor 1 minus Baseline, (C) Monitor 2 minus Baseline. Increased time delays only, showing preferentially induced orientated fractures.

Monitor 2 minus Baseline time-lapse response exhibits a diffusion of the 2-07 well anomalies just nine days after its stimulation. The time for the reservoir to reach pressure equilibrium, for pressure to propagate and for fractures to close on the proppant may happen over a longer period then previously hypothesized. Longer term monitoring may be necessary to properly characterize these changes within the reservoir.

4.6 Shear-wave Splitting Compared with Microseismic

Microseismic monitoring of the hydraulic stimulations was used to compare and correlate to the shear-wave splitting time-lapse differences. Before a comparison can be made between the two methods of hydraulic fracturing monitoring, differences between seismic shear-wave splitting and microseismic monitoring must be addressed. Microseismic events mostly represent the shear failures created by the increase in pore pressure during the hydraulic stimulation which may be less then 0.01% of the hydraulic fracture energy. On the other hand, the magnitude of shear-wave splitting represents the open fracture density (HTI - single fracture set) or the difference in fracture densities ($e_2 - e_1$) (orthorhombic - two fracture sets). Although comparisons can be made regarding hydraulic energy displacement, the mechanisms creating the results are different and cannot be directly compared.

Combining the two monitoring methods while understanding their differences can lead to more successful analysis of the hydraulic stimulations. Hydraulic fracture parameters, such as direction, length, geometric complexity, effective stimulated volume and effective permeability may be better constrained. In the following figures, microseismic event location results from the 9-07 vertical well monitor (Figure 1.12) have been overlaid on the calculated shear-wave splitting maps. The shear-wave splitting color bar has been altered to a different color gradation but the scale remains the same as previous figures.

The microseismic monitoring of the hydraulic stimulation of horizontal 2-07 well results in very few events but correspond to significant increases in shear-wave splitting magnitudes (Figure 4.8). Events may be biased to large shear-slip events as suggested by the magnitude vs. event-tool distance plot (Figure 1.13). Two linear features are interpreted in the microseismic event clouds (Figure 4.9). The northern linear feature corresponds to an area of low shear-wave splitting magnitude and the orientation coincides with dominant fracture orientation determined in the shear-wave splitting analysis (Figure 4.3). This feature could represent the conduit pathway to the areas of higher shear-wave splitting magnitude. The linear anomaly near Stage 2 trends in the regional S_{Hmax} direction along the expected orientation of induced fractures, close to the same as suggest by the shear-wave splitting results. Within the area of highest shear-wave splitting magnitude, the microseismic events are disperse. Combining the fracture orientation from shear-wave splitting analysis, the magnitude of shear-wave splitting, the microseismic event cloud seem to follow the expected failure theory of hydraulic fractures connecting the orthogonal fracture set. The lack of microseismic events for some stages may be due to tensile opening of the natural orthogonal fracture set.

Microseismic monitoring of the hydraulic stimulation of horizontal 7-07 well exhibits a significantly larger number of microseismic events, especially at the toe of the wellbore (Figure 4.10), compared to the 2-07 well. This increase in microseismic energy is not mapped in the shear-wave splitting magnitudes. Tighter and more consistent linear features are observed in the microseismic event clouds (Figure 4.11). Linear microseismic event clouds,

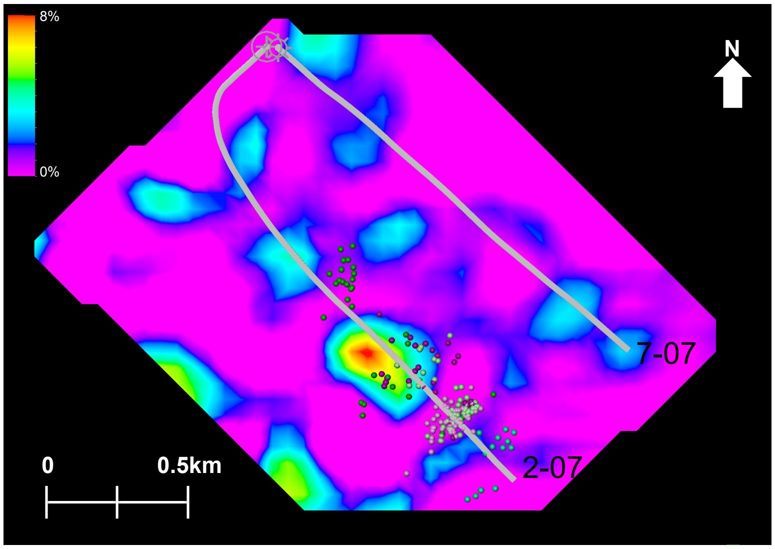

Figure 4.8: Total microseismic solution and Monitor 1 minus Baseline shear-wave splitting.

towards the heel of the well correspond to increased shear-wave splitting and follow dominant fracture orientation determined in the shear-wave splitting analysis (Figure 4.5). The nine abnormally high magnitude microseismic events (Figure 1.13) correspond to the highest density event cloud which extends southeast towards an area of increased shear-wave splitting near the 2-07 well. High magnitude events typically are caused by massive shear failures of in-situ faulted zones; this supports the interpretation of the wrench fault lineament.

4.7 Correlation to Production Data

In this section, the microseismic and shear-wave splitting results are correlated to the stage-by-stage gas production contributions. The assumption is that the percent of total gas production is related to the connected fracture permeability and reflects the hydraulic stimulation success.

From the estimated stimulated reservoir volume or the microseismic event density of the microseismic monitoring, no direct correlation to the spinner production data for each perforation location is apparent (Figure 4.12). As an example, the high concentration of microseismic events at the toe (Stage 1) of the 7-07 well may not be an indication of the

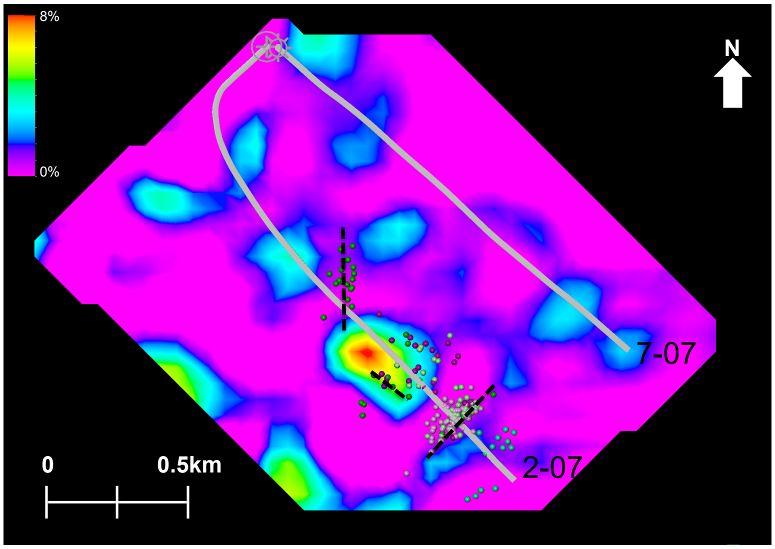

Figure 4.9: Total microseismic solution and Monitor 1 minus Baseline shear-wave splitting with interpreted fracture azimuths.

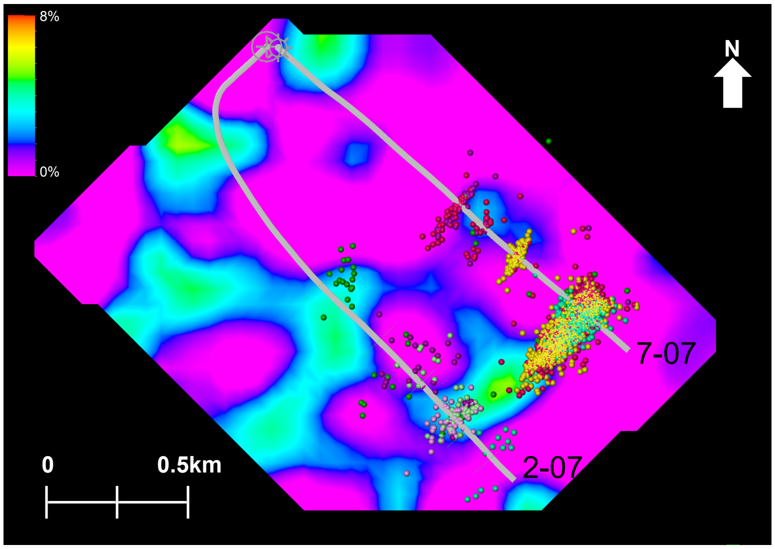

Figure 4.10: Total microseismic solution and Monitor 2 minus Baseline shear-wave splitting.

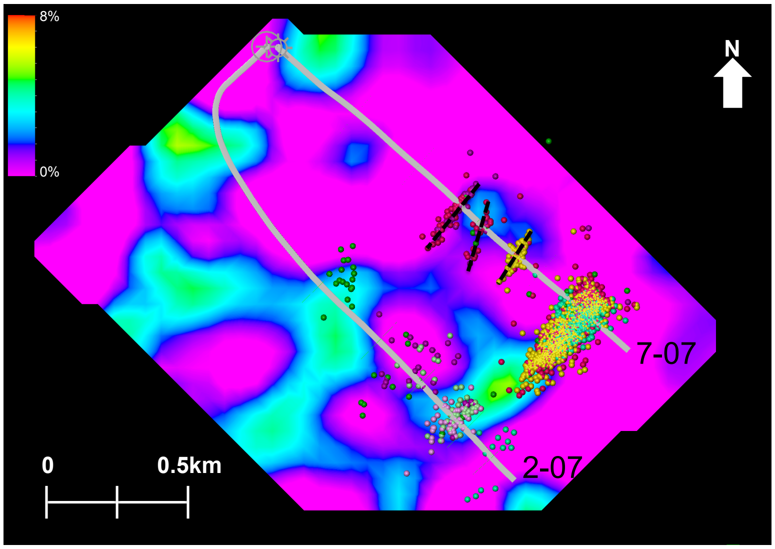

Figure 4.11: Total microseismic solution and Monitor 2 minus Baseline shear-wave splitting with interpreted fracture azimuths.

highest effective permeability as compared to other hydraulic stages. This result supports the observation by Maxwell et al. (2008) that microseismic events correspond to fast shear failures (quick breaks) and account for less then 0.01% of the energy input into the hydraulic fracture treatment. Due to this conclusion, microseismic monitoring may not be detecting the energy released during the creation of tensile fracture opening that could be related to the effective stimulated volume.

Alternatively, shear-wave splitting analysis may better relate to the final effective fracture permeability created during the hydraulic stimulation (Figure 4.13). For this correlation the induced shear-wave splitting anomalies are assumed related to the propped fracture networks providing permeable flow paths to the well bore. Based on the shear-wave splitting monitoring of the 2-07 well (Monitor1 minus Baseline in Figure 4.13), percent total gas flow is loosely related to the shear-wave splitting anomaly magnitude. The loose correlation between shear-wave splitting and production could be due to the pressure leakoff apparent just nine days later in the Monitor 2 survey (Figure 4.7 (C)).

The overall induced shear-wave splitting anomalies (Monitor 2 minus Baseline in Figure 4.13 (B)) were interpreted to be related to the hydraulic stimulation success and the

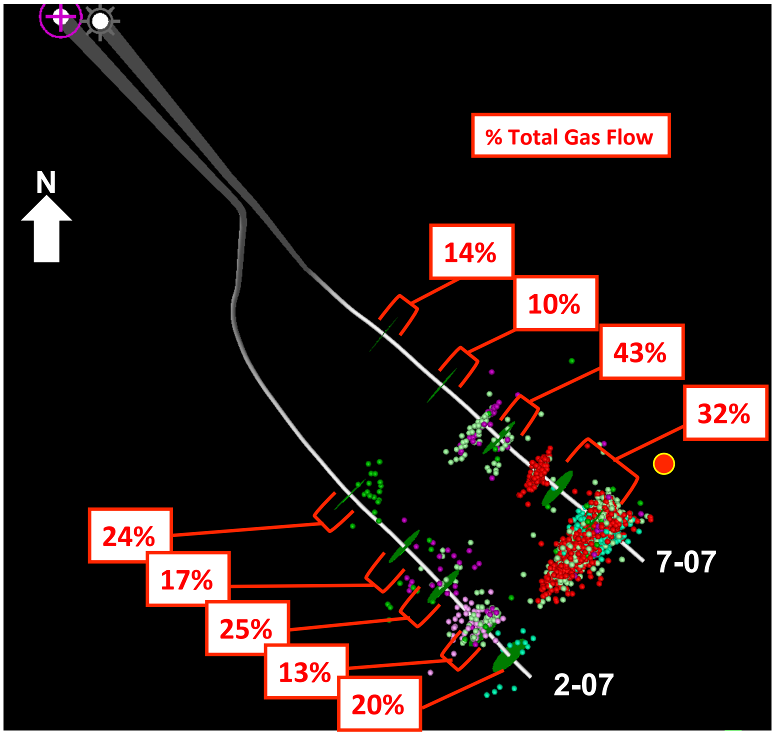

Figure 4.12: Total microseismic solution and production data. Spinner production data are labelled by frac stage and represented as percentage of total gas flow.

effective stimulated volume. The low magnitude of shear-wave splitting near the 7-07 well may relate to the fact 2-07 produced 39% more gas than the 7-07 well. The hydraulic fracturing response measured is different between shear-wave splitting monitoring and microseismic monitoring but better correlates to the production in the shear-wave splitting response. The Stage 2 production of the 2-07 well is due to its proximity to the N-E trending interpreted fault lineament near the toe of the well. Stage production was not accurately represented by in the microseismic event locations and densities either because tensile failures are below the detectable threshold or because they are considered aseismic.

4.8 Alternative Interpretations

Although it is believed the presented conclusions best represent the Montney Shale reservoir characterization, the interpretations in this study are based on multiple assumptions. Due to these imposed limitations, multiple interpretations are possible by placing different

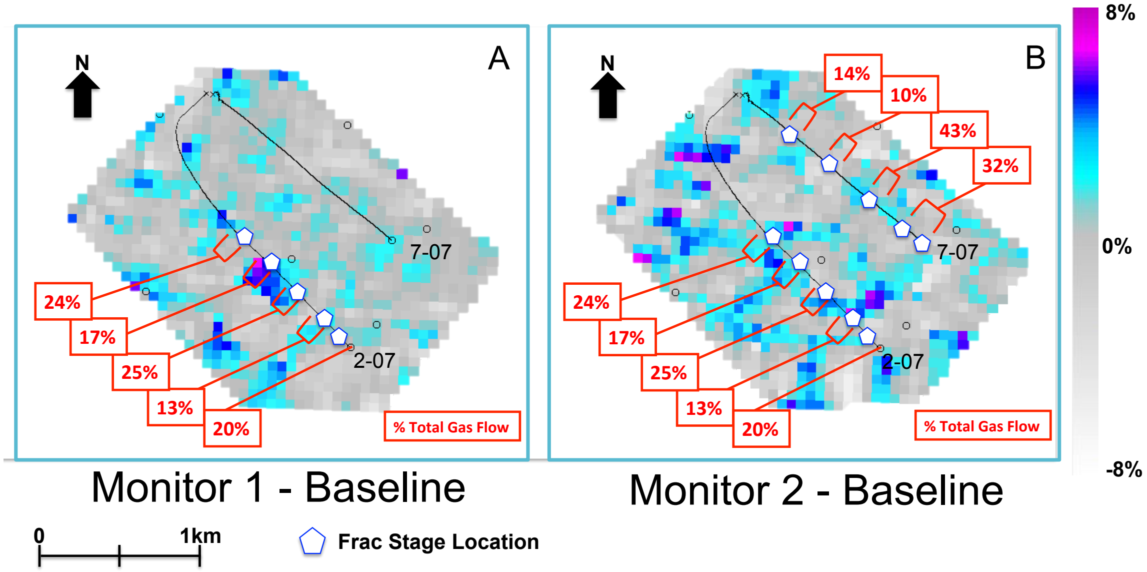

Figure 4.13: Map view of the shear-wave splitting averaged over the Montney reservoir interval. Spinner production data are labelled by frac stage and represented as percentage of total gas flow. (A) Shear-wave splitting difference between Monitor 1 and Baseline, after the stimulation of the 2-07 well. (B) Shear-wave splitting difference between Monitor 2 and Baseline, after the total stimulation of wells 2-07 and 7-07.

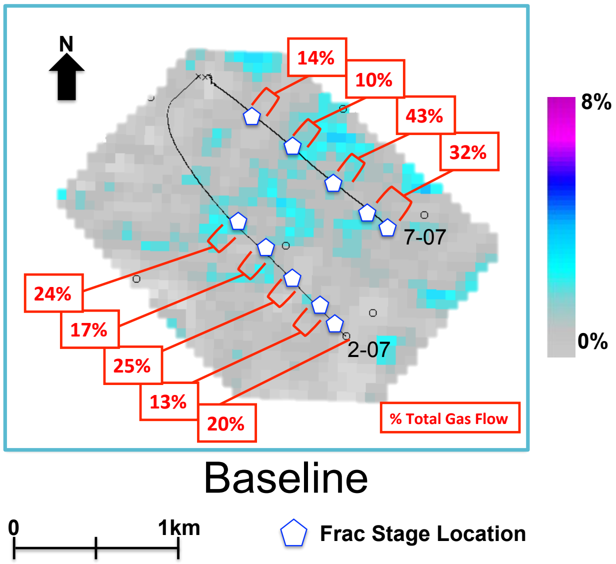

Figure 4.14: Map view of the Baseline shear-wave splitting averaged over the Montney reservoir interval. Spinner production data are highlighted by frac stage and represented as percentage of total gas flow.

weights on the data collected. Some of the ambiguities that exist are discussed below.

First, the differential horizontal stress ratio is assumed to not contribute significantly to the measurable shear-wave splitting. Locations of concentrated stress could exhibit the same shear-wave splitting behavior by altering the compliances. These stress perturbations around fractures are not accounted for in the shear-wave splitting analysis and the differential stresses could decrease the shear-wave splitting, reducing the interpreted fracture density.

The non-unique shear-wave splitting calculation could have multiple interpretations for the cause of such results. The shear-wave splitting interpretation ambiguities are:

- fracture set properties are not recovered separately (difference in crack densities $(e_2 - e_1)$)
- HTI is a special case of orthorhombic symmetry (no second fracture set $(e_1 = 0)$; therefore, $\gamma^{(1)}$=0 and $\gamma^{(s)} = \gamma^{(2)}$)
- two sets of orthogonal fractures with equal crack densities $(e_2 = e_1)$ appear isotropic ($\gamma^{(s)}$=0)
- two nonorthogonal fractures of equal crack densities $(e_2 = e_1)$ represent orthorhombic symmetry (Tsvankin, 2012a), and the S_1-wave polarizes in the direction between the two fracture orientations (Figure 4.15 (right))
- multiple nonorthogonal fracture sets represent orthorhombic symmetry, and the S_1-wave polarizes in the dominant effective fracture set orientation (Vasconcelous and Grechka, 2007)
- crack density (e) is related to the number of cracks per unit volume times the mean cubed crack length; therefore, a high concentration of small cracks is indistinguishable from a small amount of large cracks (Martin and Davis, 1987).

Analysis of time-lapse changes in the shear-wave splitting (Section 4.5) did not consider negative values. Negative values of shear-wave splitting in Monitor 2 minus Baseline could be due to the creation of a complex fracture networks, causing the shear-wave splitting magnitude to become less in Monitor 2 than in the Baseline survey. Figure 4.16 shows these negative shear-wave splitting differences for the total stimulation effect of both horizontal wells. Notice the color scale is now 0 to -4% with the majority of the values equal to zero or are positive (clipped). The negative anomalies magnitudes are less than the previous positive difference maps and many of the magnitudes are below the shear-wave splitting sensitivity and considered seismic noise.

Results from the monitor surveys are assumed to image the hydraulic stimulations but the shear-wave splitting monitoring shows a diffusive pressure behavior near the 2-07 well just nine days after stimulation occurred. Reduction of shear-wave splitting magnitude in the main anomaly (Figure 4.11 may suggest the closing of the fractures on the proppant. Alternatively, hydraulic energy may be opening and connecting fractures beyond the typical distances imaged from microseismic monitoring. Therefore, the overall effective stimulated volume is only visible after pressure equilibrium has been reached and could require longer term monitoring of the reservoir.

4.9 Interpretation Conclusion

Natural fractures and faults, imaged from the Baseline converted-wave seismic survey and shear-wave splitting, were observed to potentially control the propagation of hydraulic stimulation energy, acting as both conduits and barriers to fracturing. Geometry of the induced fracture network follow the dominant natural fracture set orientation which varies between the two orthogonal fracture sets, causing the fracturing to be asymmetric around the wellbore. The ability of time-lapse shear-wave splitting analysis to image both shear and tensile fracture opening provides a better method to determine the hydraulic stimulation success then microseismic monitoring alone. In conclusion, shear-wave splitting anomalies are assumed to reflect the effective stimulated volume.

Differences in the overall production between the two horizontal wells appear related to differences of magnitude and area of the shear-wave splitting anomalies, specifically the 2-07 well has higher shear-wave splitting magnitude. Individual stage production correlates to the overall shear-wave splitting anomalies, except for the effect on an interpreted fault. In comparison, microseismic monitoring appears to correlate less to the overall and individual stage production data.

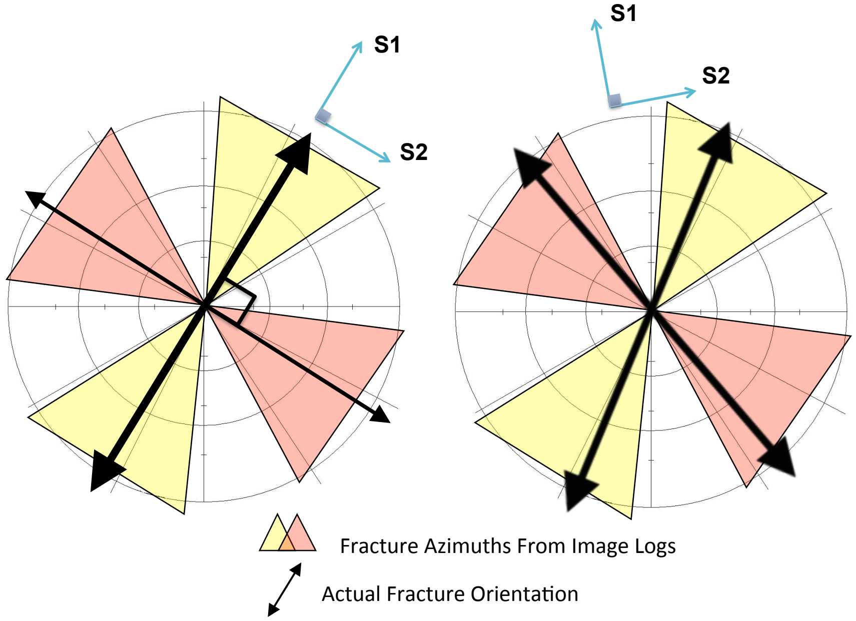

Figure 4.15: Left - Orthorhombic symmetry, two orthogonal fracture sets, one with higher density (represented as arrow scale). Right - Orthorhombic symmetry, two non-orthogonal fracture sets, with equal density.

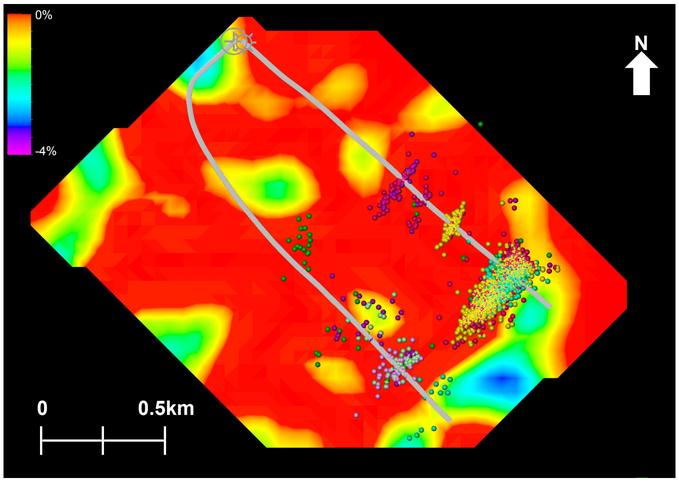

Figure 4.16: Map view of the negative shear-wave splitting after both hydraulic fracture treatments.

CHAPTER 5

CONCLUSIONS AND RECOMMENDATIONS

This study explores different scales of investigation to characterize the Montney Shale reservoir in the Pouce Coupe Field. Borehole scale geomechanics, microseismic monitoring, time-lapse multicomponent seismic and production data were integrated to determine the controlling factors of achieving economic production. The methodologies and conclusions built from this analysis should be transferable to other study areas.

Analysis of the time-lapse, converted-wave seismic data showed the feasibility of shear-wave splitting to characterize and monitor the fracturing within the reservoir interval. The polarization of the fast PS-wave (PS_1-wave) and the time delay between the PS_1- and PS_2-waves provide a quantitative measurement of the dominant fracture orientation and difference in fracture density ($\gamma^{(s)}$ proportional to $(e_1 - e_2)$), respectively.

The use of converted-wave data to determine the degree of anisotropy within the reservoir relied on some key aspects of the processing sequence developed by Sensor Geophysical and integratively refined in conjunction with myself. The improvements include: innovative methods to better determine vector fidelity using the RADAR method, improved pre-stack shear-wave splitting analysis and layer stripping by maximizing energy on the radial component, and enhancements to the time-lapse simultaneous processing for increased repeatability using NRMS-guided simultaneous processing.

5.1 Conclusions

The following conclusions were drawn from this study:

- Two dominant roughly orthogonal natural fracture sets were independently determined from Montney image logs and shear-wave splitting analysis, one roughly parallel to the regional maximum horizontal stress direction (N40^0E) and an orthogonal set.

- Before hydraulic stimulations, the natural fracture sets resulted in a measured shear-wave splitting magnitude of 2-3%, following the trends of the previously interpreted fault lineaments (Figure 4.2).

- Hydraulic fracture stimulations resulted in a shear-wave splitting magnitude increase up to 8%. The induced shear-wave splitting anomalies were mostly restricted to natural fractures, as witnessed by the consistent polarization of the fast PS-wave between the Baseline and monitoring surveys (Figure 4.6).

- Natural fractures, depending on their orientation and density, acted as either conduits or barriers to the propagation of hydraulic stimulation energy.

- Due to the detection limitations of microseismic monitoring (detected microseismic mainly correspond to shear-failure events), an accurate determination of the effective stimulated reservoir was not viable by this method.

- In comparison to microseismic monitoring, shear-wave splitting anomalies were interpreted to best represent the effective stimulated volume because of the strong correlation to production anomalies determine by the stage-by-stage spinner production data (Figure 4.13).

Going beyond the statistical engineering approach of maximizing the number of drilled wells per area, detailed reservoir characterization holds significant value if incorporated in the exploration and development phases, potentially reducing the number of uneconomical producing wells. Characterizing the natural fractures and their failure tendencies can help drive the development of such a reservoir because fracture characteristics seemed to govern hydraulic stimulation success. Baseline characterization could potentially drive the project forward with reduced risk and increased production success by incorporating the pre-exiting reservoir conditions into the development strategy. The data required to preform a multiscale, multidisciplinary study was insignificant in cost compared to the drilling and stimulation of a single horizontal well. Acquisition of the multicomponent seismic surveys cost about equivalent to the two total well stimulations.

From an interpretation of the multicomponent seismic reservoir characterization and monitoring, microseismic monitoring and the borehole scale geomechanics, the best development strategy can be determined, including the optimal drilling target (laterally and vertically), the azimuth of the well and perforation locations and stimulation parameters.

Moving forward with the Montney Shale characterization, all further analysis must consider the previously determined reservoir properties, hydraulic stimulation response and data limitations. Specifically, observations of the two orthogonal fracture sets (orthorhombic symmetry) and the witnessed fracture failure characteristics (both shear and tensile failures). Additionally, the consideration of the microseismic event detection limitations and ambiguity in the surface seismic data interpretation while determining the effective stimulated volume.

5.2 Recommendations

To further characterize this shale reservoir the following recommended analyses should entail:

- Conducting seismic inversion for rock properties; derivation of a seismic version of the Rock Quality Index (RQI)

- Conducting a further microseismic analysis beyond the conventional interpretation perform in this study (moment tensor inversion and frequency-magnitude relationship (b-value)). Also, incorporate time strain rates by combining injection rates with fracture failures measured using microseismic monitoring

- Undertaking amplitude variation with azimuth (AVAZ) and velocity variations with azimuth (VVAZ) processing and analysis for the pure compressional-wave (PP-wave) fracture characterization

- Fracture detection independently analyzed using NMO ellipses of both P- and S-waves, as analyzed by Vasconcelous and Grechka (2007).

REFERENCES CITED

Atkinson, J. (2010). Multicomponent time-lapse monitoring of two hydraulic fracture stimulations in an unconventional reservoir, pouce coupe, canada. Master's thesis, Colorado School of Mines.

Atkinson, J. and T. Davis (2011). Multi-component time-lapse monitoring of two hydraulic fracture stimulations in the pouce coupe field unconventional reservoir. *First Break 29*(10), 91–97.

Bakulin, A., V. Grechka, and I. Tsvankin (2000). Estimation of fracture parameters from reflection seismic data-part ii: Fractured models with orthorhombic symmetry. *Geophysics 65*(6), 1803–1817.

BMO (2011, October). British columbia montney gas - top economic performer.

Cary, P. (2002). Detecting false indications of shear-wave splitting. In *72nd Annual Internatation Meeting, Society of Exploration Geophysicists*, Volume 21 of *Expanded Abstracts*, pp. 1014–1017.

Cipolla, Maxwell, and Downie (2011). A practical guide to interpreting microseismic measurements. Society of Petroleum Engineers.

Davey, H. (2012). Geomechanical characterization of the montney shale northwest alberta and northeast british columbia, canada. Master's thesis, Colorado School of Mines.

Davies, G., T. Moslow, and M. Sherwin (1997). The lower triassic montney, west-central alberta. *Bulletin of Canadian Petroleum Geology 45*(4), 474–505.

Davis, T. and B. Benson (2013). The role of wrench faults and fractures in creating "sweet spots" in tight gas exploration and production at rulison field, colorado. Will appear in "Application of Structural Methods to Rocky Mountain Hydrocarbon Exploration and Development".

Grossman, J. and R. Couzens (2012, November). Preserving sensor vector fidelity using automated multicomponent receiver-azimuth detection. *The Recorder 37*(9), 46–52.

Grossman, J. and C. Steinhoff (2013). Integration of multicomponent time-lapse processing and interpretation: Focus on shear-wave splitting analysis integration of multicomponent time-lapse processing and interpretation: Focus on shear-wave splitting analysis integration of multicomponent time-lapse processing and interpretation: Focus on shear-wave splitting analysis. *The Leading Edge 32*(1), 32–38.

Hardage, B., M. DeAngelo, P. Murray, and D. Sava (2011). *Multicomponent Seismic Technology*, Volume 18. Geophysical References Series.

Landrø, M. (1999, November-December). Repeatability issues of 3-d vsp data. *Geophysics 64*(6), 1673–1679.

Li, X. and J. Grossman (2012). A stable criterion for shear wave splitting analysis. GeoConvention: Vision.

Li, X., K. Lazorko, P. Cary, and G. Margrave (2011). Simultaneous time-lapse processing for optimal repeatability. Research Report 23, CREWES.

Lumley, D. (2003). 4d seismic data processing issues and examples. *SEG Expanded Abstracts 22*(1), 1394–1397.

Martin, M. and T. Davis (1987). Shear-wave birefringence: A new took for evaluating fractured reservoirs. *Geophysics: The leading edge of exploration 6*(10), 22–28.

Maxwell, S., Schemta, Campbell, and Quirk (2008, September). Microseismic deformation rate monitoring. SPE Annual Technical Conference and Exhibition.

Mei, S. (2009). New insights on faults in the peace river arch region, northwest alberta, based on existing well log data and refined trend surface analysis. *Canadian Journal of Earth Sciences 46*, 41–46.

Terrell, M. (2004). *Fracture Permeability Characterization at Weyburn Field: From Shear Wave Anisotropy Through Flow Simulation.* Ph. D. thesis, Colorado School of Mines.

Tsvankin, I. (1997a). Anisotropic parameters and p-wave velocity for orthorhombic media. *Geophysics 62*(4), 1292–1309.

Tsvankin, I. (1997b). Reflection moveout and parameter estimation for horizontal transverse isotropy. *Geophysics 62*(2), 614–629.

Tsvankin, I. (2012a). Personal communication.

Tsvankin, I. (2012b). *Seismic signatures and analysis of reflection data in anisotropic media* (3 ed.). Society of Exploration Geophysicists.

Tsvankin, I. and V. Grechka (2011). *Seismology of Azimuthally Anisotropic Media and Seismic Fracture Characterization*. Number 17 in Geophysical Reference Series. Society of Exploration Geophysicists.

Vasconcelous, I. and V. Grechka (2007, March-April). Seismic characterization of multiple fracture sets at rulison field, colorado. *Geophysics 72*(2), B19–B30.

Warpinski (2009). Integrating microseismic monitoring with well completions, reservoir behavior and rock mechanics. Society of Petroleum Engineers.